

Quadratic serendipity element shape functions on general planar polygons

Juan Cao^{a,b,*}, Yi Xiao^{a,b}, Yanyang Xiao^c, Zhonggui Chen^d, Fei Xue^{a,b}, Xiaodong Wei^e, Yongjie Jessica Zhang^f

^a School of Mathematical Sciences, Xiamen University, Xiamen, 361005, China

^b Fujian Provincial Key Laboratory of Mathematical Modeling and High-Performance Scientific Computation, Xiamen University, Xiamen, 361005, China

^c School of Information Engineering, Nanchang University, Nanchang, 330031, China

^d School of Informatics, Xiamen University, Xiamen, 361000, China

^e Institute of Mathematics, Ecole Polytechnique Fédérale de Lausanne, Lausanne 1015, Switzerland

^f Department of Mechanical Engineering, Carnegie Mellon University, Pittsburgh, PA 15213, USA

Received 11 October 2021; received in revised form 25 January 2022; accepted 30 January 2022

Available online 19 February 2022

Abstract

This paper proposes a method for the construction of quadratic serendipity element (QSE) shape functions on planar convex and concave polygons. Existing approaches for constructing QSE shape functions are linear combinations of the pair-wise products of generalized barycentric coordinates with linear precision, restricted to the convex polygonal domain or resort to numerical optimization. We extend the construction to general polygons with no more than three collinear consecutive vertices. This is done by defining coefficients of the linear combination as the oriented area of triangles with vertices from the polygonal domain, which can be either convex or concave. The proposed shape functions possess linear to quadratic precision. We prove the interpolation error estimates for mean value coordinate-based QSE shape functions on convex and concave polygonal domains satisfying a set of geometric constraints for standard finite element analysis. We also tailor a polygonal mesh generation scheme that improves the uniformity and avoids short edges of Voronoi diagrams for their use in the QSE-based polygonal finite element computation. Numerical tests for the 2D Poisson equations on various domains are presented, demonstrating the optimal convergence rates in both the L^2 -norm and the H^1 -seminorm.

© 2022 Elsevier B.V. All rights reserved.

Keywords: Polygonal finite element methods; Generalized barycentric coordinates; Polygonal mesh generation

1. Introduction

The finite element method (FEM) is the most widely used tool for solving partial differential equations in applied mathematics, engineering, and scientific computing. To solve a boundary-value problem, the FEM subdivides the domain of interest into small and simple finite elements, which conventionally are triangles/quadrilaterals in 2D or tetrahedra/hexahedra in 3D [1]. Although allowing for simple and efficient implementation, these well-established

* Corresponding author at: School of Mathematical Sciences, Xiamen University, Xiamen, 361005, China.

E-mail address: juancao@xmu.edu.cn (J. Cao).

finite elements require complex remeshing when the simulation domain undergoes changes such as merging, cutting, and fracturing. The process of remeshing can be difficult and very time-consuming.

One possibility to circumvent the aforementioned problem is to generalize the FE methods to general polygonal or polyhedral meshes. As has been shown in the literature, polygonal finite elements possess several advantages over classical finite elements. For example, the polygonal FEM [2] can directly process elements cutting from triangular or rectangular elements without resorting to remeshing. Polygonal finite elements also provide more flexibility by allowing a more general family of element types beyond triangles and quadrilaterals. It has been shown that polygonal finite elements can better capture the propagation of cracks and crack branching [3,4] and are capable of handling to a wide range of irregular geometries [5,6]. Besides, they are also suitable for modeling complex domains with adaptive mesh refinement [7].

There is a wide body of literature that considers the construction of polygonal finite elements. Among these works, a popular idea is to use the so-called generalized barycentric coordinates (GBCs) as the polygonal shape functions. Barycentric coordinates provide perhaps the most convenient way to linearly interpolate data associated with the vertices of a simplex. In computer graphics, numerous extensions of barycentric coordinates on simplices have been proposed for polygons [8], polyhedra [9] and curves [10]. Along with the advances of GBCs in computer graphics, polygonal FEMs based on GBCs have concomitantly gained much momentum. There are a wide variety of applications available that showcase the contributions of different polygonal FEMs in approximation of PDE [11–13], fracture modeling [14] and topology optimization [15].

Oftentimes, bases with the higher-order approximation property on polygonal domains are desired in practical applications. For example, for basis functions in functional data [16] or PDE approximation [11–13], GBCs with higher-order approximation property provide space/accuracy advantages over elements based on the basis with only linear precision. However, most GBCs suffer from only linear precision, which limits their wide use in polygonal FEMs. To date, the topic of constructing higher-order basis functions on polygonal domain has received only limited attention [9,11–13,17].

The goal of this paper is to explicitly construct quadratic serendipity element (QSE) shape functions over general polygonal domains. We construct QSE shape functions by pairwise-product GBCs, which are then grouped through linear combinations while preserving the basic properties of GBCs. It should be pointed out that similar ideas of constructing higher-order spline space using GBCs (including the classical barycentric coordinates) have already been studied in [9,11–13]. However, these methods are either restricted to convex polygonal/polyhedral domains [9,12,13], or they are defined implicitly such that they need to solve an optimization problem [11]. This paper offers a simple yet efficient method to construct QSE shape functions with quadratic completeness on both convex and concave polygons using mean value coordinates. The specific contributions of this paper are as follows:

- We provide an easy procedure to explicitly construct QSE shape functions on both convex and concave polygonal domains. In addition to the approximation property, the constructed QSE shape functions inherit most properties of GBCs, such as the partition of unity and the Kronecker-delta property.
- We prove that the mean value coordinates-based QSEs provide optimal order of convergence for interpolation error on polygonal domains satisfying a set of geometric conditions.
- We present an efficient mesh generation method for generating uniform meshes free of short edges and large angles for their use in the QSE based polygonal finite element computation.

The remainder of this paper is organized as follows. In Section 2, we construct the QSE shape functions on general polygons, discuss the properties of proposed functions and propose geometric constraints for each polygonal element. In Section 3, we generate the polygonal meshes according to the proposed geometric constraints. In Section 4, we solve the Poisson equations using our QSE shape functions and polygonal meshes and study the convergence rates in numerical experiments. We conclude the paper in Section 5.

2. Construction of quadratic serendipity element shape functions on general polygons

In this section, the QSE shape functions over general polygons are discussed. We first provide a brief overview of barycentric coordinates over triangles and their generalizations to polygonal domains. Then, we present the explicit construction of QSE shape functions on general polygons. Finally, we prove interpolation error estimates for the mean value coordinate-based QSEs on polygonal domains satisfying a set of geometric constraints.

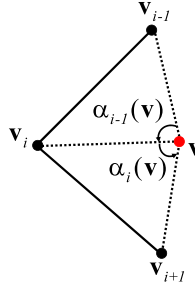


Fig. 1. Signed angles used to compute mean value coordinates.

2.1. Generalized barycentric coordinates

Barycentric coordinates over triangles. Barycentric coordinates over triangles, also known as “triangular coordinates”, were introduced by Möbius in 1827 [18]. Given a triangle defined by its three vertices $\{\mathbf{v}_1, \mathbf{v}_2, \mathbf{v}_3\}$, each point \mathbf{v} located inside this triangle can be represented as a unique convex combination of three vertices as follows:

$$\mathbf{v} = \sum_{i=1}^3 \phi_i(\mathbf{v}) \mathbf{v}_i,$$

where

$$\phi_1(\mathbf{v}) = \frac{A(\mathbf{v}, \mathbf{v}_2, \mathbf{v}_3)}{A(\mathbf{v}_1, \mathbf{v}_2, \mathbf{v}_3)}, \quad \phi_2(\mathbf{v}) = \frac{A(\mathbf{v}_1, \mathbf{v}, \mathbf{v}_3)}{A(\mathbf{v}_1, \mathbf{v}_2, \mathbf{v}_3)}, \quad \text{and} \quad \phi_3(\mathbf{v}) = \frac{A(\mathbf{v}_1, \mathbf{v}_2, \mathbf{v})}{A(\mathbf{v}_1, \mathbf{v}_2, \mathbf{v}_3)}$$

are the barycentric coordinates associated with vertices $\mathbf{v}_1, \mathbf{v}_2$ and \mathbf{v}_3 , respectively, and $A(\mathbf{v}_i, \mathbf{v}_j, \mathbf{v}_k)$ is the signed area of the triangle $[\mathbf{v}_i, \mathbf{v}_j, \mathbf{v}_k]$. Consider a triangle $[\mathbf{v}_1, \mathbf{v}_2, \mathbf{v}_3]$, its barycentric coordinates possess the following basic properties:

- Partition of unity, i.e., $\sum_{i=1}^3 \phi_i = 1$;
- Kronecker-delta property, i.e., $\phi_i(\mathbf{v}_j) = \delta_{ij}$;
- Linear precision property, i.e., $\mathbf{v} = \sum_{i=1}^3 \phi_i(\mathbf{v}) \mathbf{v}_i$.

Triangular coordinates provide perhaps the most convenient way to linearly interpolate data associated with the vertices of triangles. Barycentric coordinates defined with respect to polygons, polyhedrals and curves are referred to as generalized barycentric coordinates (GBCs). While they have been enriched with different constraints, such as harmonicity [19], positiveness [20], regularity [21] and locality [22], to name a few, most GBCs retain the basic properties of barycentric coordinates, including the partition of unity, Kronecker-delta property, linear precision property, and smoothness within the domain. In the following, we briefly introduce the mean value coordinates which we will use for higher-order basis construction. For a more detailed discussion of the generalized barycentric coordinates, interested readers are referred to a thorough survey [23].

Mean value coordinates. A typical example of GBCs on arbitrary polygons is the mean value coordinates (MVCs) [8]. Consider a simple polygon (that does not self-intersect and has no holes) with n vertices $\{\mathbf{v}_1, \mathbf{v}_2, \dots, \mathbf{v}_n\}$ ordered counter-clockwise. The interior, boundary and closure of the region bounded by the polygon are denoted by P , ∂P and \bar{P} , respectively. We define a weight function $w_i(\mathbf{v})$ on P for each vertex \mathbf{v}_i as follows:

$$w_i(\mathbf{v}) = \frac{\tan(\alpha_i(\mathbf{v})/2) + \tan(\alpha_{i-1}(\mathbf{v})/2)}{\|\mathbf{v}_i \mathbf{v}\|}, \quad (1)$$

where $\alpha_i(\mathbf{v})$ is the signed angle at point \mathbf{v} with respect to the triangle $[\mathbf{v}, \mathbf{v}_i, \mathbf{v}_{i+1}]$ and $\|\mathbf{v}_i \mathbf{v}\|$ is the distance between point \mathbf{v}_i and \mathbf{v} ; see Fig. 1. The so-called MVCs are defined as the normalized weight functions

$$\phi_i(\mathbf{v}) = \frac{w_i(\mathbf{v})}{\sum_{k=1}^n w_k(\mathbf{v})}. \quad (2)$$

MVCs allow the polygonal domain P to be non-convex. They are well defined for all points in P and extended naturally to ∂P .

In addition to MVCs, there is a considerable amount of work that generalizes the barycentric coordinates to general polygons, such as bi-harmonic coordinates [19], maximum entropy coordinates [20], green coordinates [24], harmonic coordinates [25], Poisson coordinates [21], power coordinates [26], blended coordinates [27], local barycentric coordinates [28], and iterative coordinates [29]. However, some of these coordinates do not possess closed-form expressions. Hence the analysis is often difficult. For example, harmonic coordinates are obtained as solutions to Laplace's equations, approximated by a numerical solver. The maximum entropy coordinates are derived from numerical optimizations, which also require quadratures and involve approximate evaluations. The construction of QSE shape functions, which we will discuss in Section 2.2, starts with any GBCs that are well defined over the given polygon. For the sake of simplicity, we will demonstrate how to create QSE shape functions using MVCs and study the interpolation properties of MVC-based QSEs in the remainder of this section.

2.2. QSE shape functions construction

Consider a simple polygon with n vertices $\{\mathbf{v}_1, \mathbf{v}_2, \dots, \mathbf{v}_n\} \subset \mathbb{R}^2$ ordered counter-clockwise and the corresponding polygonal domain P ; see Fig. 2. We assume that the polygon is non-degenerate, i.e., no three consecutive vertices of the polygons are collinear. Starting from a given set of GBCs $\{\phi_i\}_{i=1}^n$ defined on \bar{P} , we construct QSE shape functions of size $2n$, $\{\psi_i, i = 1, \dots, 2n\}$ by following the recent work of Rand et al. [12].

In [12], the development of QSE shape functions on a polygonal domain includes three steps: order elevation, function reduction, and Kronecker-delta property preservation, where quadratic functions in each step are linear combinations of the quadratic functions obtained in the previous step. However, their construction is restricted to convex polygons since the computation of linear combination coefficients in Step 2 is restricted to convex polygons. In the following, we provide a different way of linear combination to define QSE shape functions on general polygons:

Step 1 (Order elevation) By pairwise multiplying ϕ_i , we obtain a set of quadratic functions $\{\mu_{i,j} := \phi_i \phi_j\}$ for $i, j = 1, \dots, n$. Since $\mu_{i,j} = \mu_{j,i}$, there are $\frac{n(n+1)}{2}$ unique functions $\{\mu_{i,i}, \mu_{i,j} | i = 1, \dots, n, j \geq i\}$ and they are assigned to vertices, edge midpoints or diagonals of the polygon. In particular, $\mu_{i,i}$ and $\mu_{i,i+1}$ are assigned to the vertex \mathbf{v}_i and the midpoint of $\mathbf{v}_i \mathbf{v}_{i+1}$, respectively, and $\mu_{i,j}$ is assigned to the diagonal $\mathbf{v}_i \mathbf{v}_j$ for $j - i > 1$. For simplicity, we denote by \mathbf{v}_{n+i} the midpoint of edge $\mathbf{v}_i \mathbf{v}_{i+1}$.

Step 2 (Function reduction) Note that functions $\mu_{i,j}$ ($j - i > 1$) always vanish on the boundary ∂P . To reduce the number of quadratic functions to $2n$, each $\mu_{i,j}$ is split into six functions and added to the quadratic functions associated with polygon vertices or edges. More precisely, $2\mu_{i,j}$ is decomposed to six functions as:

$$2\mu_{i,j} = c_{i,j}^{i,i} \mu_{i,j} + c_{i,j}^{j,j} \mu_{i,j} + 2c_{i,j}^{i,i-1} \mu_{i,j} + 2c_{i,j}^{i,i+1} \mu_{i,j} + 2c_{i,j}^{j,j-1} \mu_{i,j} + 2c_{i,j}^{j,j+1} \mu_{i,j}, \quad (3)$$

where the functions on the right-hand side only differ in coefficients,

$$\begin{aligned} c_{i,j}^{i,i} &= \frac{A(\mathbf{v}_{i-1}, \mathbf{v}_j, \mathbf{v}_{i+1})}{A(\mathbf{v}_{i-1}, \mathbf{v}_i, \mathbf{v}_{i+1})}, & c_{i,j}^{j,j} &= \frac{A(\mathbf{v}_{j-1}, \mathbf{v}_i, \mathbf{v}_{j+1})}{A(\mathbf{v}_{j-1}, \mathbf{v}_j, \mathbf{v}_{j+1})}, \\ c_{i,j}^{i,i-1} &= \frac{A(\mathbf{v}_j, \mathbf{v}_i, \mathbf{v}_{i+1})}{2A(\mathbf{v}_{i-1}, \mathbf{v}_i, \mathbf{v}_{i+1})}, & c_{i,j}^{j,j-1} &= \frac{A(\mathbf{v}_i, \mathbf{v}_j, \mathbf{v}_{j+1})}{2A(\mathbf{v}_{j-1}, \mathbf{v}_j, \mathbf{v}_{j+1})}, \\ c_{i,j}^{i,i+1} &= \frac{A(\mathbf{v}_{i-1}, \mathbf{v}_i, \mathbf{v}_j)}{2A(\mathbf{v}_{i-1}, \mathbf{v}_i, \mathbf{v}_{i+1})}, & c_{i,j}^{j,j+1} &= \frac{A(\mathbf{v}_{j-1}, \mathbf{v}_j, \mathbf{v}_i)}{2A(\mathbf{v}_{j-1}, \mathbf{v}_j, \mathbf{v}_{j+1})}, \end{aligned} \quad (4)$$

and $A(\mathbf{v}_i, \mathbf{v}_j, \mathbf{v}_k)$ is the signed area of triangle $[\mathbf{v}_i, \mathbf{v}_j, \mathbf{v}_k]$; see Fig. 2(b). The resulting six quadratic functions are added to the quadratic functions associated with vertices $\mathbf{v}_i, \mathbf{v}_j$, midpoint of edges $\mathbf{v}_{i-1} \mathbf{v}_i, \mathbf{v}_i \mathbf{v}_{i+1}, \mathbf{v}_{j-1} \mathbf{v}_j, \mathbf{v}_j \mathbf{v}_{j+1}$, respectively; see Fig. 2(a). As a result, we obtain $2n$ quadratic functions

$$\xi_{i,i} = \mu_{i,i} + \sum_{j,j-i>1} c_{i,j}^{i,i} \mu_{i,j},$$

and

$$\xi_{i,i+1} = \mu_{i,i+1} + \sum_{j,j-i>1} c_{i,j}^{i,i+1} \mu_{i,j} + \sum_{j,j-i-1>1} c_{i+1,j}^{i+1,i} \mu_{i+1,j},$$

where $i = 1, \dots, n$, $\xi_{i,i}$ and $\xi_{i,i+1}$ are associated with vertices \mathbf{v}_i and midpoints of edges $\mathbf{v}_i \mathbf{v}_{i+1}$, respectively.

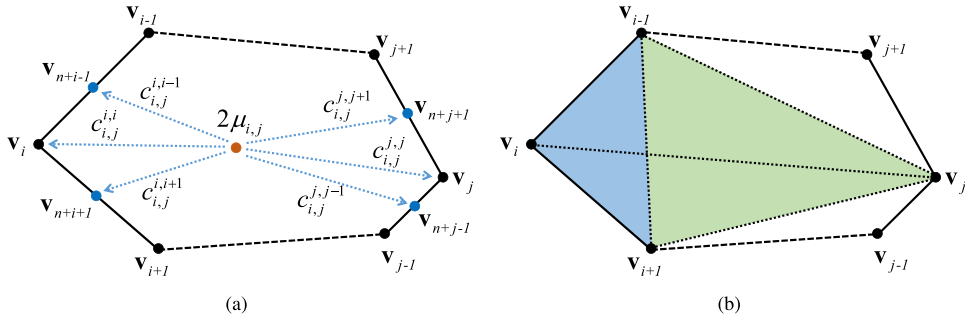


Fig. 2. Redistribution of an internal function $2\mu_{i,j}$ ($j - i > 1$). (a) Decomposition of $2\mu_{i,j}$ into six functions, which are then added to the functions associated with certain vertices/midpoints; and (b) areas of triangles $[v_{i-1}, v_i, v_{i+1}]$ (blue) and $[v_{i-1}, v_j, v_{i+1}]$ (green). (For interpretation of the references to color in this figure legend, the reader is referred to the web version of this article.)

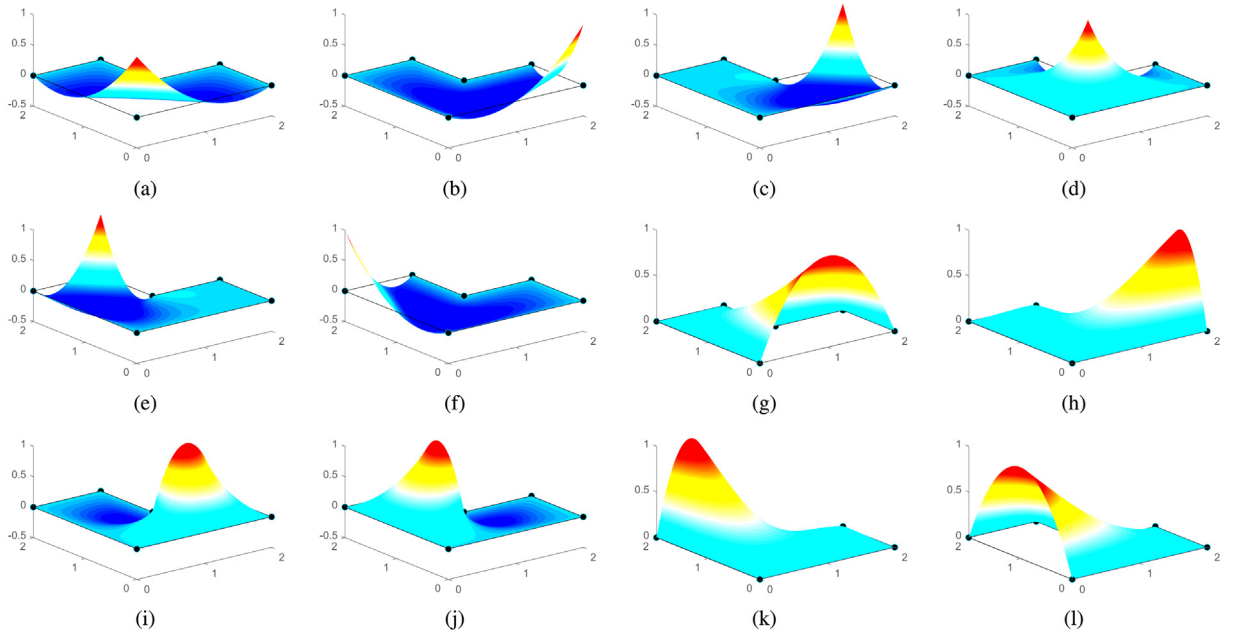


Fig. 3. QSE shape functions on an L -shaped domain. (a–f) QSE shape functions associated with polygon vertices; and (g–l) QSE shape functions associated with midpoints of edges of the L -shaped polygon.

Step 3 (Kronecker-delta property preservation) To ensure the Kronecker-delta property, we further reform the $2n$ quadratic functions $\xi_{i,i}$ and $\xi_{i,i+1}$ as follows

$$\psi_i = \xi_{i,i} - \xi_{i,i+1} - \xi_{i-1,i} \quad \text{and} \quad \psi_{n+i} = 4\xi_{i,i+1}, \quad i = 1, \dots, n, \quad (5)$$

where ψ_i and ψ_{n+i} are associated with vertices v_i and midpoints of edges $v_i v_{i+1}$, respectively.

Examples of the proposed QSE shape functions on an L -shaped domain are shown in Fig. 3. Assume that the GBCs used to construct QSE shape functions satisfy the partition of unity, the linear precision, and the Kronecker-delta property, QSE shape functions $\{\psi_i\}_{i=1}^{2n}$ satisfy the following properties:

(1) **Partition of unity:** $\sum_{i=1}^{2n} \psi_i = 1$;

(2) **Kronecker-delta property:** $\psi_i(v_j) = \delta_{i,j}$ for $i, j = 1, \dots, 2n$;

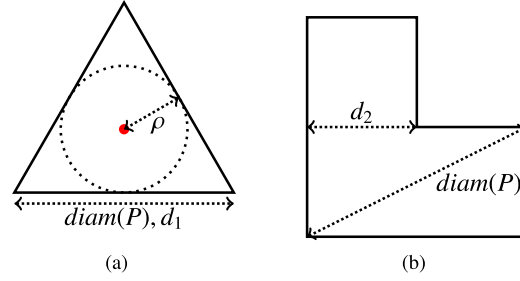


Fig. 4. Notations for diameter, radius of the maximum inscribed circle and the minimum distance between two non-adjacent edges of a polygonal domain P .

(3) **Linear precision:** $\sum_{i=1}^{2n} \psi_i \mathbf{v}_i = \mathbf{v}$;

(4) **Quadratic precision:** $\sum_{i=1}^{2n} \psi_i \mathbf{v}_i \mathbf{v}_i^T = \mathbf{v} \mathbf{v}^T$.

It can be easily verified that the constructed shape functions satisfy the Kronecker-delta property and the partition of unity. The proof of the linear and quadratic precision properties is available in [Appendix A](#).

2.3. Interpolation error estimates for MVC-based QSE shape functions

This section derives the interpolation error estimates for MVC-based QSE shape functions. The interpolation error estimate allows us to show the optimal convergence rate of applying MVC-based QSEs in finite element systems under some assumptions on geometrical properties of the polygonal mesh. Our proof of error estimates is compatible with the standard analysis of the FEM; please refer to textbooks, e.g., [30] for the full details on the setting. Numerical experiments in Section 4.2 will experimentally verify that the polygonal FEM based on our MVC-based QSE shape functions achieves expected optimal convergence rates, i.e., 3 for the L^2 -norm error and 2 for the H^1 -seminorm error.

Our error estimate is contingent upon the polygonal mesh satisfying a set of geometric quality constraints. We consider a simple polygon element with vertices $\{\mathbf{v}_1, \mathbf{v}_2, \dots, \mathbf{v}_n\}$ ordered counter-clockwise and the corresponding polygonal domain P . Denote by $\text{diam}(P)$ the diameter of P , i.e., the maximum distance between any two points in P , and denote by ρ the radius of the maximum inscribed circle in P ; see Fig. 4(a). The chunkiness parameter of a convex polygonal domain P is defined by $\gamma(P) = \text{diam}(P)/\rho$. The polygonal domain P satisfies the following geometry constraints:

- (C1.A) **Bounded chunkiness parameter and bounded minimum edge length (for convex polygon):** If P is convex, there exist $d_1 > 0$ and $\gamma^* > 0$, such that for all $i \in \{1, 2, \dots, n\}$, $\|\mathbf{v}_i \mathbf{v}_{i+1}\| \geq d_1$ and $\gamma(P) \leq \gamma^*$; see Fig. 4(a).
- (C1.B) **Bounded minimum distance between non-adjacent edges (for concave polygon):** If P is concave, there exists $d_2 > 0$, such that $\forall \mathbf{x} \in \mathbf{e}_i$ and $\forall \mathbf{y} \in \mathbf{e}_j$, $\|\mathbf{x} \mathbf{y}\| \geq d_2$, where \mathbf{e}_i and \mathbf{e}_j are two non-adjacent edges; see Fig. 4(b).
- (C2) **Bounded interior angle:** there exists $\beta > 0$, such that $\beta \leq |\angle(\mathbf{v}_{i-1}, \mathbf{v}_i, \mathbf{v}_{i+1})| \leq \pi - \beta$ for $i = 1, \dots, n$, where $\angle(\mathbf{a}, \mathbf{b}, \mathbf{c}) \in (-\pi, \pi]$ is the signed angle rotating clockwise around \mathbf{b} from \mathbf{ba} to \mathbf{bc} .
- (C3) **At most one concave vertex:** there exists at most one vertex $\mathbf{v}_i, i \in \{1, \dots, n\}$, such that $\angle(\mathbf{v}_{i-1}, \mathbf{v}_i, \mathbf{v}_{i+1}) < 0$.
- (C4) **Maximum vertex count:** there exists $n^* \geq 3$, such that $n \leq n^*$.

C1 (consisting of C1.A and C1.B) gives a uniform lower bound $d = \min\{d_1, d_2\}$ for the length of edges for both convex and concave polygons. Geometric constraint C3 is reasonable and easy to satisfy. The computational domain

can be partitioned into dense enough cells by Voronoi tessellation, where only boundary cells can be concave and have at most one concave vertex.

Upon the proposed geometric constraints, we consider the interpolation error estimates. Our approach of interpolation error estimates for MVC-based QSEs follows the method in [31], which carries out a similar program for the MVCs on the convex polygonal domain proposed for use in the finite element context. We first introduce some notations. Given a multi-index $\nu = (\nu_1, \nu_2)$ with ν_1, ν_2 non-negative integers and a point $\mathbf{v} = (x, y)$, we define $\mathbf{v}^\nu = x^{\nu_1} y^{\nu_2}$ and $D^\nu u(\mathbf{v}) = \partial^{|\nu|} u(\mathbf{v}) / \partial x^{\nu_1} \partial y^{\nu_2}$, where $|\nu| = \nu_1 + \nu_2$. The Sobolev space $H^k(P)$ over P is defined as

$$H^k(P) = \{u : \int_P |D^\nu u(\mathbf{v})|^2 d\mathbf{v} < \infty, \forall |\nu| \leq k\}.$$

The H^k -seminorm $|\cdot|_{H^k(P)}$ and the H^k -norm $\|\cdot\|_{H^k(P)}$ defined over P are

$$|u|_{H^k(P)} = \sqrt{\int_P \sum_{|\nu|=k} |D^\nu u(\mathbf{v})|^2 d\mathbf{v}}, \quad \|u\|_{H^k(P)} = \sqrt{\sum_{m=0}^k |u|_{H^m(P)}^2}, \quad k = 0, 1, 2, \dots$$

The interpolation error estimates for QSE shape functions that we seek have the following form:

$$\|u - Iu\|_{H^1(P)} \leq C_e \text{diam}(P)^2 |u|_{H^3(P)}, \quad \forall u \in H^3(P), \quad (6)$$

where C_e is a constant to be found, I is the interpolation operator on P defined as

$$Iu = \sum_{i=1}^{2n} u(\mathbf{v}_i) \psi_i(\mathbf{v}),$$

with $\{\psi_i\}_{i=1}^{2n}$ the set of QSE shape functions, and $u(\mathbf{v}_i)$ is the interpolation coefficient of ψ_i .

To obtain the interpolation error estimates in Eq. (6) for QSE shape functions, we first bound the H^1 -norms of QSE shape functions on domains satisfying constraints C1–C4 and with the unit diameter in Theorems 1–3. Then, we apply Bramble–Hilbert lemma [32] and Sobolev embedding theorem [33,34] to derive the interpolation error estimates on a polygonal domain with the unit diameter in Theorem 4. Finally, we derive the interpolation error estimates on a polygonal domain with any scales of diameter in Theorem 5.

Theorem 1. *Let P be a polygonal domain with $\text{diam}(P) = 1$ and satisfying geometric constraints C1–C2, then the coefficients defined in Eq. (4) for the QSE shape function construction are uniformly bounded, i.e., there exists a constant C_c such that*

$$|c_{i,j}^{a,b}| \leq C_c \quad \text{for } j - i > 1, a \in \{i, j\}, \text{ and } b \in \{a - 1, a, a + 1\}.$$

Proof. Constraint C1 (consisting of C1.A and C1.B) implies that the edges of both convex and concave polygons are bounded, i.e., $d \leq \|\mathbf{v}_i \mathbf{v}_{i+1}\| \leq 1$. Note that the coefficients are the ratios of signed areas of triangles, where the denominator is always the signed area of the triangle formed by consecutive points from the polygonal domain. Then, for each pair of i and j satisfying $j - i > 1$, we have

$$|c_{i,j}^{i,i}| = \frac{|A(\mathbf{v}_{i-1}, \mathbf{v}_j, \mathbf{v}_{i+1})|}{|A(\mathbf{v}_{i-1}, \mathbf{v}_i, \mathbf{v}_{i+1})|} = \frac{\|\mathbf{v}_{i-1} \mathbf{v}_j\| \cdot \|\mathbf{v}_j \mathbf{v}_{i+1}\| \sin |\angle(\mathbf{v}_{i-1}, \mathbf{v}_j, \mathbf{v}_{i+1})|}{\|\mathbf{v}_i \mathbf{v}_{i-1}\| \cdot \|\mathbf{v}_i \mathbf{v}_{i+1}\| \sin |\angle(\mathbf{v}_{i-1}, \mathbf{v}_i, \mathbf{v}_{i+1})|} \leq \frac{1}{d^2 \sin \beta} = C_c.$$

Similarly, we can bound the other five coefficients by the constant C_c . \square

The following theorem proves that MVCs and their gradients are bounded by a uniform constant C_g under the geometric constraints C1–C4.

Theorem 2. *Let P be a polygonal domain with $\text{diam}(P) = 1$ and satisfying geometric constraints C1–C4, then the MVCs ϕ_i defined in Eqs. (1) and (2) and their gradients $\nabla \phi_i$ are uniformly bounded, i.e., for all $\mathbf{v} \in P$, there exists a constant C_g such that*

$$|\phi_i(\mathbf{v})| \leq C_g, \quad |\nabla \phi_i(\mathbf{v})| \leq C_g, \quad i \in \{1, 2, \dots, n\}.$$

Proof. The proof is provided in Appendix B. \square

Remark 1. The uniform bounds on GBCs (including Wachspress coordinates, Sibson coordinates, Harmonic coordinates, and MVCs) on convex polygons have been provided in [31,35]. Among these GBCs, only the MVCs can be explicitly computed for non-convex polygons and applied to our QSE shape functions. In fact, convexity is dispensable for providing gradient bounds of MVCs. We provide sufficient geometric constraints C1–C4 for bounding the H^1 -norm of the proposed QSE shape functions and the corresponding analysis in Appendix B. The proposed QSE shape function may also be uniformly bounded on more general polygonal domains, such as those with more than one concave vertex. However, the current proof in Appendix B cannot be extended to such general cases straightforwardly. We need further study to provide rigorous proof for the bounds of the proposed QSE shape functions on more general domains in the future.

The following theorem implies that the H^1 -norms of QSE shape functions ψ_i on P with $\text{diam}(P) = 1$ and satisfying geometric constraints C1–C4 can be bounded by a uniform constant.

Theorem 3. *Let P be a polygonal domain with $\text{diam}(P) = 1$ and satisfying geometric constraints C1–C4, then the H^1 -norm of QSE shape functions constructed in Section 2.2 are uniformly bounded, i.e., there exists a constant C_q such that*

$$\|\psi_i(\mathbf{v})\|_{H^1(P)} \leq C_q, \quad i \in \{1, 2, \dots, 2n\}.$$

Proof. We denote $C_q = 12(1 + \frac{n^{*2}-3n^*}{2}C_c)C_g^2$, and we have

$$\|\psi_i\|_{H^1(P)} \leq 4\|\xi_{i,j}\|_{H^1(P)} \leq 4(1 + \frac{n^{*2}-3n^*}{2}C_c)\|\mu_{i,j}\|_{H^1(P)} \leq 12(1 + \frac{n^{*2}-3n^*}{2}C_c)C_g^2 \leq C_q.$$

Theorem 4. *Let P be a polygonal domain satisfying geometric constraints C1–C4 with $\text{diam}(P) = 1$, then for all $u \in H^3(P)$, there exists a constant C_e such that*

$$\|u - Iu\|_{H^1(P)} \leq C_e|u|_{H^3(P)}.$$

Proof. The proof is provided in Appendix C. \square

Theorem 5. *Let P be a polygonal domain satisfying geometric constraints C1–C4, then the interpolation error estimates in Eq. (6) hold, i.e., for all $u \in H^3(P)$, there exists a constant C_e such that*

$$\|u - Iu\|_{H^1(P)} \leq C_e \text{diam}(P)^2 |u|_{H^3(P)}. \quad (7)$$

Proof. The proof is provided in Appendix C. \square

According to the standard Galerkin FEM, the interpolation error estimate usually gives the bounds of approximation error between the exact solution u and the numerical solution u_h . For the sake of completeness, the estimate of approximation error in the H^1 -seminorm according to the Lax–Milgram Lemma [30] is given in the case of the elliptic equation as

$$|u - u_h|_{H^1(P)} \leq \|u - u_h\|_{H^1(P)} \leq C_{h,1} \|u - Iu\|_{H^1(P)}$$

with $C_{h,1} > 0$ a constant real number. Similarly, the estimate of approximation error in the L^2 -norm according to the Aubin–Nitsche Lemma [30] is given as

$$\|u - u_h\|_{H^0(P)} \leq C_{h,2} \text{diam}(P) \|u - u_h\|_{H^1(P)}$$

with $C_{h,2} > 0$ a constant real number. Together with the relation (7) obtained in Theorem 5, we have that the approximation error is controlled by

$$|u - u_h|_{H^1(P)} \leq C_{e,1} \text{diam}(P)^2,$$

and

$$\|u - u_h\|_{H^0(P)} \leq C_{e,2} \text{diam}(P)^3,$$

with constant real numbers $C_{e,1}, C_{e,2} > 0$. Hence, optimal-order convergence of approximation error in L^2 -norm, and H^1 -seminorm can be preserved theoretically.

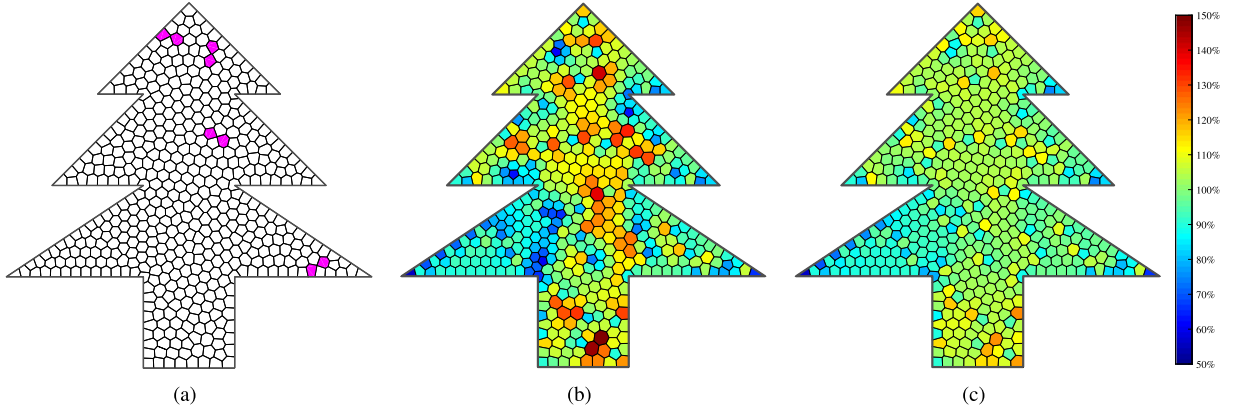


Fig. 5. Removal of short edges and preservation of uniformity in a CVT mesh. (a) The input CVT mesh, with cells containing short edges marked in magenta; (b) the result from [41], where the short edges are removed but the uniformity may be destroyed; and (c) our uniform mesh is free of short edges. For each cell in (b&c), the color indicates the ratio of cell's area to the average area c defined in Eq. (11) according to the color bar in the right side.

3. Implementation of polygonal FEM

In this section, we address two important implementation aspects of the proposed method, that is, polygonal mesh generation and numerical integration. Our polygonal mesh generation is based on the geometry constraints C1–C4 proposed in Section 2.3.

3.1. Mesh generation and optimization

Generally, polygonal mesh generation is based on the Voronoi diagram and its properties. Most polygonal FEMs directly use Voronoi tessellation. For example, the centroidal Voronoi tessellation (CVT) method [36–38] and the maximal Poisson-disk sampling (MPS) method [39] have been used to generate Voronoi meshes with uniformly distributed seed points. On the other hand, some other polygonal FEMs first generate primal triangulation and then exploit the duality of Voronoi diagram and Delaunay triangulation to generate polygonal meshes [40].

It is widely known in computational mechanics community that the accuracy and stability of numerical computation highly depend on the element shapes and sizes. Meshes with poorly shaped elements may yield an ill-conditioned linear system and thus lead to an inaccurate solution. However, the quality criteria for polygonal meshes are not well understood as those for triangular meshes. As discussed in the previous section, elements with small angles, flat angles or short edges should be avoided in our polygonal meshes as they cause a blowup in the coefficients for constructing QSE shape functions. Such short edges can be eliminated by merging their endpoints. However, edge collapsing destroys the uniformity of a Voronoi diagram and alters the topology of a polygonal mesh. In many applications, elements are desired to be as regular in shape and uniform in size as possible. To achieve this goal, we first generate polygonal meshes by CVT and then improve the quality of polygonal meshes by exploiting a modified version of the variational mesh optimization method in [41]. Note that, elements with small angles or short edges may occur around the domain boundary if the boundary contains small angles or short edges. Flat angles can be easily avoided by adding two seed points in the domain close enough to the flat angle vertex and symmetrical to the angle bisector of the angle and then fixing them during the later Voronoi mesh optimization. For simplicity, we assume that the domain boundary is free of small angles, flat angles, or short edges after this.

3.1.1. CVT mesh generation

CVT is a special Voronoi diagram whose seeds coincide with the mass center of corresponding regions. Given a set of seed points $S = \{\mathbf{s}_i\}_{i=1}^n$ on a domain $\Omega \subset \mathbb{R}^2$, the CVT restricted on the domain Ω satisfies

$$\mathbf{s}_i = \frac{\int_{V(\mathbf{s}_i) \cap \Omega} \mathbf{x} p(\mathbf{x}) d\mathbf{x}}{\int_{V(\mathbf{s}_i) \cap \Omega} \mathbf{x} d\mathbf{x}}, i \in \{1, \dots, n\},$$

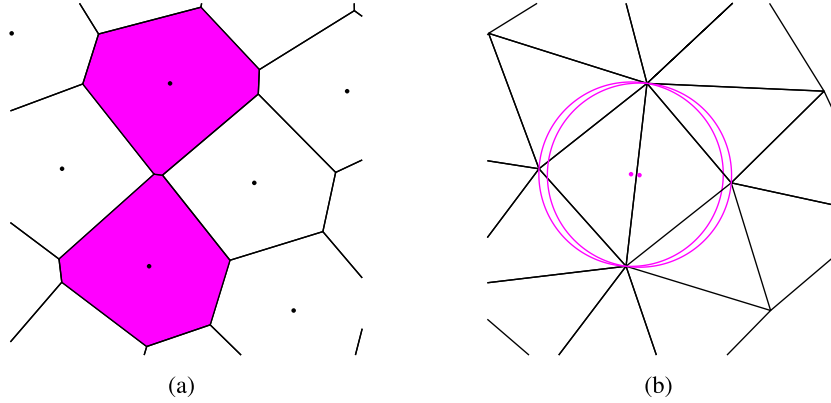


Fig. 6. A short edge in the Voronoi diagram and the dual Delaunay triangulation. (a) Voronoi diagram with cells containing short edges filled in magenta; and (b) circumcenters of triangles in the dual Delaunay triangulation (marked in magenta), which are close to each other, are the endpoints of the short edge in (a). (For interpretation of the references to color in this figure legend, the reader is referred to the web version of this article.)

where $V(\mathbf{s}_i)$ is the Voronoi cell of \mathbf{s}_i and $p(\mathbf{x})$ is a given density function that controls the seed point distribution. CVT can be obtained by minimizing the following energy function,

$$E_{\text{CVT}}(S) = \sum_{i=1}^n \int_{V(\mathbf{s}_i) \cap \Omega} p(\mathbf{x}) \|\mathbf{x} \mathbf{s}_i\|^2 d\mathbf{x}. \quad (8)$$

The CVT energy function can be minimized by the popular Lloyd's method [42], which has linear convergence. Here, we use the L-BFGS method [43] that converges faster in computing stable CVTs [36]. To generate uniform polygonal cells, we set $p(\mathbf{x}) \equiv 1$ and do not allow seed points on boundaries in general, which yields a high-quality CVT mesh free of flat and small angles. However, it may contain undesired short edges; see Fig. 5(a) for an example. We will discuss their treatment in the next section. Note that if the domain is concave, the domain boundary is clipped by the edges of Voronoi cells. As a consequence, short edges on the concave corner may be introduced. To remove short edges and avoid introducing cells with more than one concave vertex, we include the concave vertices as the seed points and fix them during minimization.

3.1.2. Removal of short edges

According to the duality property of a Voronoi diagram, vertices \mathbf{x}_i of Voronoi cells are circumcenters of their Delaunay triangles, and the edge $(\mathbf{x}_i, \mathbf{x}_j)$ of a Voronoi cell is formed by circumcenters of two adjacent Delaunay triangles; see Fig. 6 for an example. Hence, to avoid short edges of Voronoi cells, we should avoid close circumcenters of adjacent Delaunay triangles. To achieve this goal, the circumcenters of Delaunay triangles are shifted towards their incenters [41]. In particular, the squared distance d from a Delaunay triangle circumcenter to the incenter is minimized upon the following energy function,

$$E_{\text{RSE}}(\mathbf{s}_1, \dots, \mathbf{s}_n) = \frac{1}{2} \sum_{t \in T} d_t^2 = \frac{1}{2} \sum_{t \in T} R_t(R_t - 2r_t), \quad (9)$$

where t is a triangle in the Delaunay triangulation T , and R_t and r_t are the circumradius and inradius, respectively. Note that the circumradius R and inradius r of a triangle $[\mathbf{s}_i, \mathbf{s}_j, \mathbf{s}_k]$ can be computed as

$$R = \frac{\|\mathbf{s}_i \mathbf{s}_j\| \cdot \|\mathbf{s}_i \mathbf{s}_k\| \cdot \|\mathbf{s}_j \mathbf{s}_k\|}{4|A(\mathbf{s}_i, \mathbf{s}_j, \mathbf{s}_k)|} \quad \text{and} \quad r = \frac{2|A(\mathbf{s}_i, \mathbf{s}_j, \mathbf{s}_k)|}{\|\mathbf{s}_i \mathbf{s}_j\| + \|\mathbf{s}_i \mathbf{s}_k\| + \|\mathbf{s}_j \mathbf{s}_k\|},$$

respectively, which can be used to simplify the form of the energy function; see Eq. (9). However, we observe that the minimizer of the energy function may destroy the uniformity of CVT as shown in Fig. 5(b), where some cells have an area much larger than the average area c . We propose adding a penalty term in the energy to better preserve uniformity while removing the short edges. The modified energy function is defined as:

$$E = E_{\text{RSE}} + \lambda E_{\text{CapVT}}, \quad (10)$$

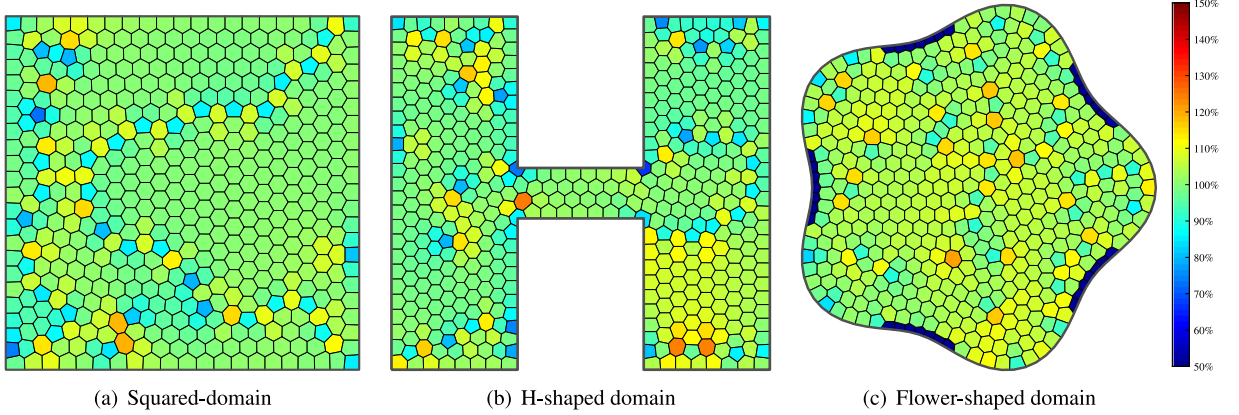


Fig. 7. Uniform meshes with 500 cells on various domains. For each cell in (a–c), the color indicates the ratio of the cell area to the average area c defined in Eq. (11) according to the color bar in the right side.

where

$$E_{\text{CapVT}}(\mathbf{s}_1, \dots, \mathbf{s}_n) = \sum_{i=1}^n \left(\int_{V(\mathbf{s}_i) \cap \Omega} d\mathbf{x} - c \right)^2 \quad (11)$$

is the penalty term that keeps the area of each cell as close to the average area $c = \frac{\text{Area}(\Omega)}{n}$ as possible, and λ is a weight to balance these two energy terms. The modified energy can be efficiently optimized using the L-BFGS method.

The modified energy function results in polygonal meshes with better quality, in the sense that cells have more uniform areas and longer shortest-edges. We find that when the weight $\lambda \in [5, 10]$, it gives satisfactory results in all our experiments. Fig. 5 shows an example of a tree-shaped domain. The input CVT mesh in Fig. 5(a) has the shortest edge of length 10^{-5} . The length of the shortest edges increases to 3.88×10^{-2} and 4.70×10^{-2} by minimizing the original energy defined in Eq. (9) and the modified energy defined in Eq. (10), respectively. Based on the improved meshes, our method leads to a decrease in the condition number. For example, the condition numbers of the stiffness matrix for solving the Poisson problem in Eq. (12) on the three different meshes for the tree-shaped domain in Fig. 5(a–c) are 8.66×10^{11} , 2.89×10^4 , and 2.55×10^4 , respectively. Three more meshes on different domains generated by our methods are shown in Fig. 7, where the polygons are colored in the same way as in Fig. 5. In Fig. 7(c), the cells marked in navy blue around the boundary have smaller areas than the interior ones, as they have seed points fixed at the concave vertices on the boundary to avoid short edges on the boundary. In Fig. 8, we generate a series of meshes (1000, 2000, 4000 cells) on a butterfly-shaped domain.

3.2. Integration

The proposed QSE shape functions are not polynomials in general. The accurate and efficient numerical integration of non-polynomial functions is an issue that has been encountered in meshfree methods [44]. At present, many researchers have used various numerical methods to obtain the integration. This paper uses the polynomial precise quadrature rules on triangles to numerically compute integrals [45]. In particular, we decompose each polygonal cell Ω_i into a set of non-intersecting triangles whose union is Ω_i by the ear clipping method [46]. Each triangle is further subdivided into 4 sub triangles as the integration cells by the 1-to-4 splits by connecting midpoints of every pair of edges to improve the integration precision. In each sub triangle, a 3-point rule is adopted to achieve degree of precision as 2. It should be pointed out that our method cannot pass the patch test because of limited accuracy inherited from the numerical integration. The proposed quadratic polygonal finite elements may pass the quadratic patch test by applying more sophisticated integration schemes, such as the derivative correction-based method [11,47]. However, the numerical results in the next section suggest that the 3-point rule is sufficient to achieve optimal convergence.

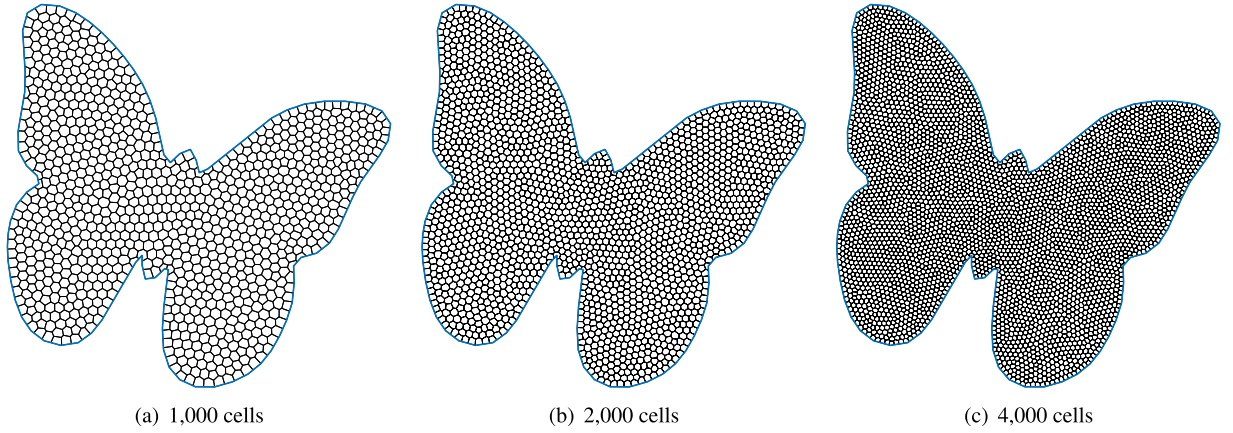


Fig. 8. Uniform meshes generated on a butterfly-shaped domain with various numbers of cells.

4. Applications in solving Poisson equations

The proposed QSE shape functions on polygonal elements can be used in various finite element applications. In particular, our proposed method allows for the quadratic method to be used on polygonal meshes with not only convex elements but also concave elements. In this section, we solve the Poisson equation on various domains. We will show that the polygonal FEM based on our QSE shape functions achieves optimal convergence rates.

4.1. 2D Poisson equations

Given a 2D domain Ω , we find a function $u(\mathbf{x})$ for the following 2D Poisson equation with the Dirichlet boundary condition:

$$\begin{cases} -\Delta u = f & \text{in } \Omega, \\ u = g & \text{on } \partial\Omega, \end{cases} \quad (12)$$

where Δ is the Laplace operator. Following the standard Galerkin approximation scheme, we first discrete the domain by the mesh generation method in Section 3.1. Then the function $u(\mathbf{x})$ is approximated by the QSE shape functions associated to vertices and midpoints of edges in the polygonal mesh as

$$u(\mathbf{x}) \approx u_h(\mathbf{x}) = \sum_{i=1}^{2n} c_i \psi_i(\mathbf{x}),$$

where c_i are the unknowns to be determined. By inserting this approximation into the weak form of the problem (12), we obtain a system of linear equations:

$$A \begin{pmatrix} c_1 \\ \vdots \\ c_{2n} \end{pmatrix} = \begin{pmatrix} f_1 \\ \vdots \\ f_{2n} \end{pmatrix} \quad \text{with} \quad A_{i,j} = \int_{\Omega} \nabla \psi_i \cdot \nabla \psi_j d\Omega \quad \text{and} \quad f_i = \int_{\Omega} f \psi_i d\Omega, \quad (13)$$

where A is the stiffness matrix. To show the convergence rate, we choose $f = -\Delta u$ and $g = u|_{\partial\Omega}$ for a certain manufactured solution u . The numerical integration used to compute Eq. (13) is performed via the quadrature rule for triangles as described in Section 3.2.

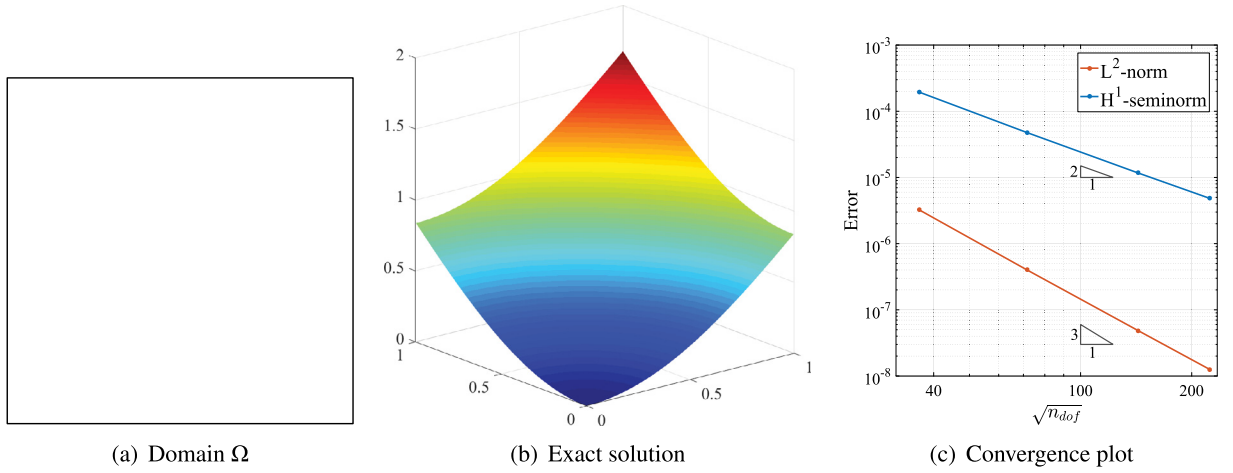


Fig. 9. Poisson problem on a square domain and approximation errors in the L^2 -norm and the H^1 -seminorm versus $\sqrt{n_{\text{dof}}}$ obtained by using our QSE shape functions.

4.2. Convergence study

In all the numerical experiments, we compute the relative error in the L^2 -norm and the H^1 -seminorm defined on the domain Ω as follows:

$$e_{L^2} = \frac{|u - u_h|_{H^0(\Omega)}}{|u|_{H^0(\Omega)}}, \quad e_{H^1} = \frac{|u - u_h|_{H^1(\Omega)}}{|u|_{H^1(\Omega)}}. \quad (14)$$

Example 1. In the first example, we consider the Poisson equation on a square domain $\Omega = [0, 1] \times [0, 1]$ with the following manufactured solution:

$$u(x, y) = x \sin x + y \sin y.$$

The domain Ω is uniformly tessellated by 250 to 10,000 polygonal cells, the polygonal mesh with 500 cells is shown in Fig. 7(a). The errors in the L^2 -norm and the H^1 -seminorm with respect to the square root of the degrees of freedom (n_{dof}) are presented in Fig. 9(c). We observe that the expected optimal convergence rates (3 for the L^2 -norm error and 2 for the H^1 -seminorm error) are achieved. As our mesh generation method tessellates the convex domain into convex cells, we can compare our method to [12], where QSE shape functions are only defined for convex elements. We find that the choice of the QSE shape functions does not affect the accuracy. For example, with 20,003 degrees of freedom, the L^2 -norm errors of [12] and our method are 5.33628×10^{-8} and 5.32347×10^{-8} , and the H^1 -seminorm errors are 1.23799×10^{-5} and 1.23622×10^{-5} , respectively.

Example 2. In the second example, we consider an H -shaped domain as shown in Fig. 10(a), with the following manufactured solution:

$$u(x, y) = 0.5e^x \sin y.$$

In this example, four concave cells are introduced at the concave corners on the boundary. We can directly define the QSE shape functions. The polygonal mesh with 500 cells on an H -shaped domain is shown in Fig. 7(b). The resulting errors in the L^2 -norm and the H^1 -seminorm with respect to the square root of n_{dof} are presented in Fig. 10, which again demonstrate the optimal approximation power of the proposed QSE shape functions.

Example 3. In the third example, we solve the Poisson problem on a flower-shaped domain with the exact solution:

$$u(x, y) = x^3 + y^3.$$

The domain and the exact solution are depicted in Fig. 11(a) and Fig. 11(b), respectively. In this example, the given domain boundary contains short edges, which cannot be removed by our mesh optimization method. In the

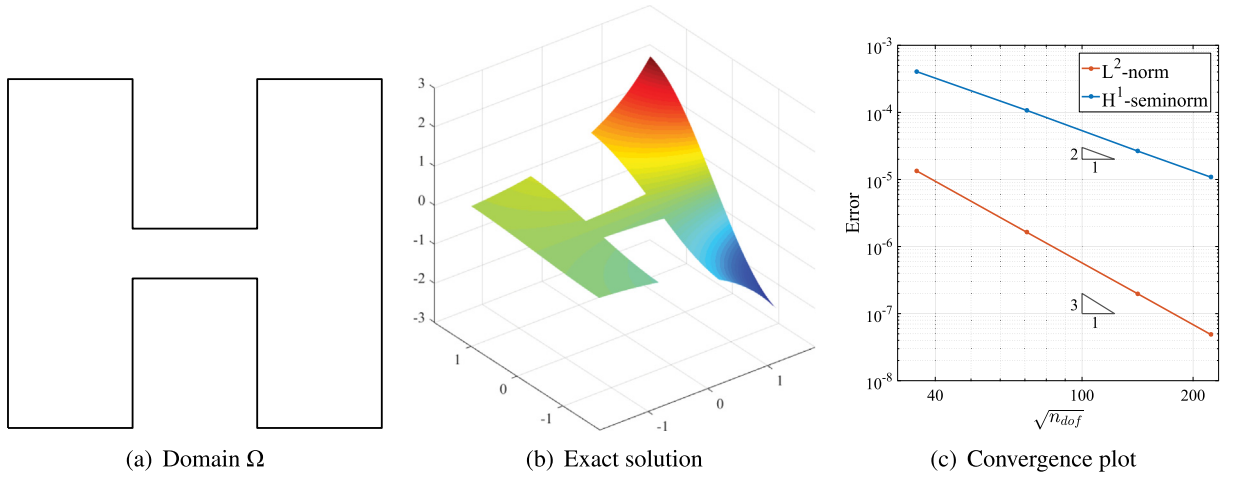


Fig. 10. Poisson problem on an H -shaped domain and approximation errors in the L^2 -norm and the H^1 -seminorm versus $\sqrt{n_{\text{dof}}}$ obtained by using QSE shape functions.

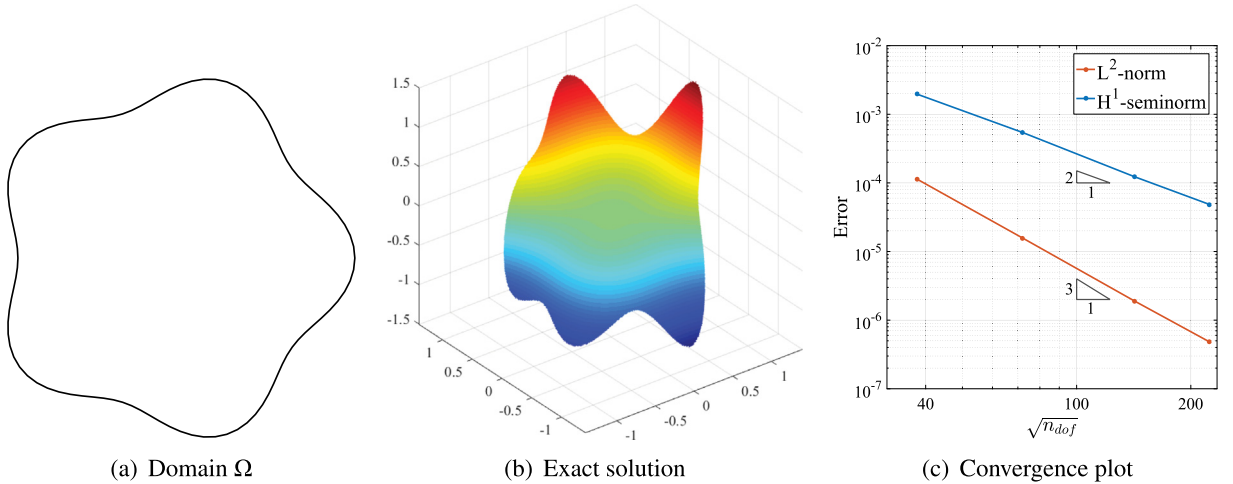


Fig. 11. Poisson problem on a flower-shaped domain and approximation errors in the L^2 -norm and the H^1 -seminorm versus $\sqrt{n_{\text{dof}}}$ obtained by using QSE shape functions.

convergence study, we create uniform meshes with the cell numbers from 250 to 10,000, such that the boundary edges have moderate length relative to the cell size. The polygonal mesh with 500 cells on a flower-shaped domain is shown in Fig. 7(c). Again, the optimal convergence rates of both errors are demonstrated in Fig. 11(c).

Example 4. In the final example, we solve the Poisson problem on a butterfly-shaped domain with the exact solution:

$$u(x, y) = xy \sin(3\pi x) \sin(3\pi y).$$

The domain and the solution are depicted in Fig. 12(a) and Fig. 12(b), respectively. In this example, 16 concave cells are introduced at the concave corners on the boundary. We create uniform meshes (see Fig. 8) and directly define the QSE shape functions. The optimal convergence rates of both errors are achieved again, as shown in Fig. 12(c).

5. Conclusion

This paper has proposed a unified construction for QSE shape functions on convex and concave polygons. In [12], QSE shape functions are represented as linear combinations of pairwise products of general barycentric

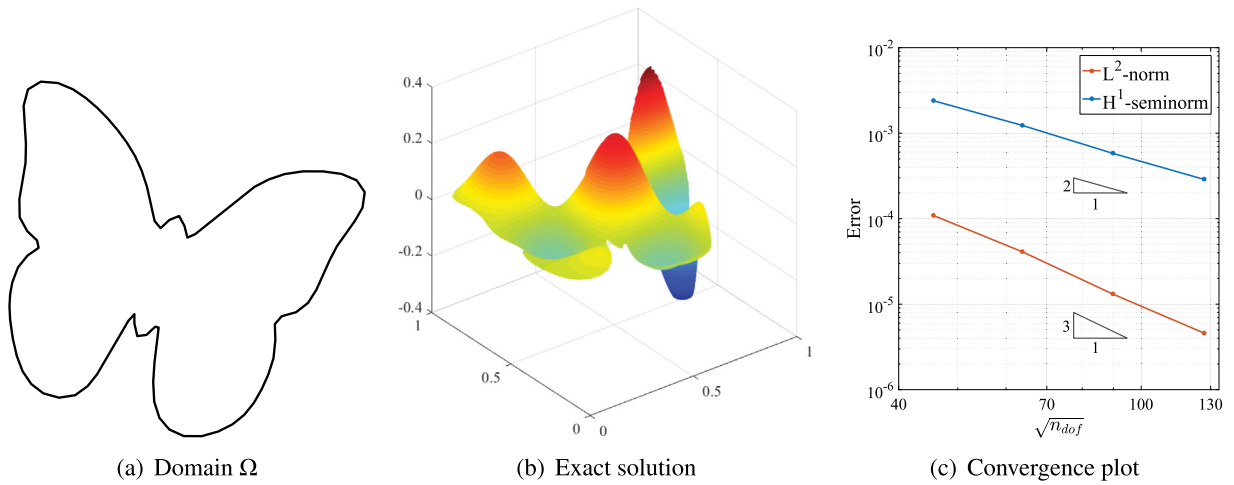


Fig. 12. Poisson problem on a butterfly-shaped domain and approximation errors in the L^2 -norm and the H^1 -seminorm versus $\sqrt{n_{\text{dof}}}$ obtained by using QSE shape functions.

coordinates defined on convex polygons. We extend QSE shape functions to general (convex and concave) polygons by expressing shape functions in terms of generalized barycentric coordinates. The coefficients in the linear combinations are well-defined by the locally oriented areas of triangles, where the polygon can be convex or concave. The constructed QSE shape functions possess constant to quadratic precision. We also provide geometric constraints on the polygonal domain and establish the interpolation error estimates for the constructed MVC-based QSE shape functions. An efficient mesh generation method has also been tailored to produce uniform polygonal meshes satisfying the polygonal domain geometry constraints. The accuracy and the convergence properties of the proposed QSE shape functions are numerically studied for 2D Poisson problems in various domains, where we observe the expected optimal convergence rate.

As the proposed QSE shape functions are rational polynomials, we triangulate polygonal cells for numerical integration and apply quadrature rules to each triangle. To achieve higher integration precision, finer integration triangles or more integration points are required. More sophisticated integration schemes, such as the corrected integration scheme, will be adopted to improve the accuracy and efficiency of our method. We also provide sufficient geometric constraints to bound the gradients of our MVC-based QSE shape functions. The proposed QSE shape functions are restricted to planar convex and concave domains, where no three consecutive points are collinear and at most one concave vertex is allowed in a given domain. The construction of QSE shape functions for polygonal domains with collinear vertices and more concave vertices needs further investigation. Besides, different geometric constraints may be required for different types of coordinates. A more detailed analysis of the geometric conditions for other types of coordinates-based QSE shape functions is an open problem for future study. Nonetheless, our method can also support adaptive refinement by specifying an appropriate non-uniform function for the density in our energy function. However, choosing proper density functions for different problems such that the adaptive meshes lead to desired convergence rates is non-trivial, which needs further investigation. Finally, benefiting from their quadratic precision property, the proposed QSE shape functions can reproduce computational domains bounded by polynomial quadratic curves and offer good accuracy to approximate other complex domains. Hence, the proposed QSEs can potentially be applied to isogeometric analysis (IGA), which is another exploration direction.

Declaration of competing interest

The authors declare that they have no known competing financial interests or personal relationships that could have appeared to influence the work reported in this paper.

Acknowledgments

The research of Juan Cao and Zhonggui Chen was supported by the National Natural Science Foundation of China (Nos. 61872308, 61972327), the Natural Science Foundation of Fujian Province of China (No. 2019J01026), the

Fundamental Research Funds for the Central Universities, China (Nos. 20720190011, 20720190063), the Xiamen Youth Innovation Funds, China (No. 3502Z20206029), and the Open Project Program of State Key Laboratory of Virtual Reality Technology and Systems, Beihang University, China (No. VRLAB2021B01). The research of Yanyang Xiao was supported by the National Natural Science Foundation of China (No. 62102174). Xiaodong Wei was partially supported by the ERC AdG project CHANGE, Switzerland n.694515 and the SNSF project HOGAEMS, Switzerland n.200021-188589. Yongjie Jessica Zhang was supported in part by the National Science Foundation, USA CMMI-1953323 and a Honda grant, Japan.

Appendix A. Proof of the linear and quadratic precision properties

According to [12], the QSE shape functions constructed in Section 2 possess constant to quadratic precision properties if the coefficients $c_{i,j}^{i,i}, c_{i,j}^{j,j}, c_{i,j}^{i,i-1}, c_{i,j}^{i,i+1}, c_{i,j}^{j,j-1}, c_{i,j}^{j,j+1}$ as in Eq. (4) satisfy the following three constraints, where we omit the subscripts i, j in the following equations to ease the notation:

$$c^{i,i} + 2c^{i,i-1} + 2c^{i,i+1} + c^{j,j} + 2c^{j,j-1} + 2c^{j,j+1} = 2; \quad (\text{A.1})$$

$$c^{i,i}\mathbf{v}_i + c^{i,i-1}(\mathbf{v}_{i-1} + \mathbf{v}_i) + c^{i,i+1}(\mathbf{v}_i + \mathbf{v}_{i+1}) + c^{j,j}\mathbf{v}_j + c^{j,j-1}(\mathbf{v}_{j-1} + \mathbf{v}_j) + c^{j,j+1}(\mathbf{v}_j + \mathbf{v}_{j+1}) = \mathbf{v}_i + \mathbf{v}_j; \quad (\text{A.2})$$

$$c^{i,i}\mathbf{v}_i\mathbf{v}_i^T + c^{i,i-1}(\mathbf{v}_i\mathbf{v}_{i-1}^T + \mathbf{v}_{i-1}\mathbf{v}_i^T) + c^{i,i+1}(\mathbf{v}_i\mathbf{v}_{i+1}^T + \mathbf{v}_{i+1}\mathbf{v}_i^T) + c^{j,j}\mathbf{v}_j\mathbf{v}_j^T + c^{j,j-1}(\mathbf{v}_j\mathbf{v}_{j-1}^T + \mathbf{v}_{j-1}\mathbf{v}_j^T) + c^{j,j+1}(\mathbf{v}_j\mathbf{v}_{j+1}^T + \mathbf{v}_{j+1}\mathbf{v}_j^T) = \mathbf{v}_i\mathbf{v}_i^T + \mathbf{v}_j\mathbf{v}_j^T. \quad (\text{A.3})$$

From Eq. (4), we have

$$c^{i,i} + 2c^{i,i-1} + 2c^{i,i+1} = 1 \quad \text{and} \quad c^{j,j} + 2c^{j,j-1} + 2c^{j,j+1} = 1.$$

It is easy to verify that Eq. (A.1) holds. We rewrite the left side of Eq. (A.2) as

$$((c^{i,i} + c^{i,i-1} + c^{i,i+1})\mathbf{v}_i + c^{i,i-1}\mathbf{v}_{i-1} + c^{i,i+1}\mathbf{v}_{i+1}) + ((c^{j,j} + c^{j,j-1} + c^{j,j+1})\mathbf{v}_j + c^{j,j-1}\mathbf{v}_{j-1} + c^{j,j+1}\mathbf{v}_{j+1}). \quad (\text{A.4})$$

Note that, from Eq. (4) we have

$$c^{i,i}\mathbf{v}_i + 2c^{i,i-1}\mathbf{v}_{i-1} + 2c^{i,i+1}\mathbf{v}_{i+1} = \mathbf{v}_j.$$

Thus, the summation in the first bracket in Eq. (A.4) becomes

$$\begin{aligned} & (c^{i,i} + c^{i,i-1} + c^{i,i+1})\mathbf{v}_i + c^{i,i-1}\mathbf{v}_{i-1} + c^{i,i+1}\mathbf{v}_{i+1} \\ &= \frac{1}{2}(c^{i,i} + 2c^{i,i-1} + 2c^{i,i+1})\mathbf{v}_i + \frac{1}{2}(c^{i,i}\mathbf{v}_i + 2c^{i,i-1}\mathbf{v}_{i-1} + 2c^{i,i+1}\mathbf{v}_{i+1}) \\ &= \frac{1}{2}\mathbf{v}_i + \frac{1}{2}\mathbf{v}_j. \end{aligned}$$

Similarly, it can be proved that

$$(c^{j,j} + c^{j,j-1} + c^{j,j+1})\mathbf{v}_j + c^{j,j-1}\mathbf{v}_{j-1} + c^{j,j+1}\mathbf{v}_{j+1} = \frac{1}{2}\mathbf{v}_i + \frac{1}{2}\mathbf{v}_j.$$

By adding the above two equations together, we get Eq. (A.2).

To prove that Eq. (A.3) holds, we first consider the first line in Eq. (A.3):

$$\begin{aligned} & c^{i,i}\mathbf{v}_i\mathbf{v}_i^T + c^{i,i-1}(\mathbf{v}_i\mathbf{v}_{i-1}^T + \mathbf{v}_{i-1}\mathbf{v}_i^T) + c^{i,i+1}(\mathbf{v}_i\mathbf{v}_{i+1}^T + \mathbf{v}_{i+1}\mathbf{v}_i^T) \\ &= \left(\frac{1}{2}c^{i,i}\mathbf{v}_i + c^{i,i-1}\mathbf{v}_{i-1} + c^{i,i+1}\mathbf{v}_{i+1}\right)\mathbf{v}_i^T + \mathbf{v}_i\left(\frac{1}{2}c^{i,i}\mathbf{v}_i^T + c^{i,i-1}\mathbf{v}_{i-1}^T + c^{i,i+1}\mathbf{v}_{i+1}^T\right) \\ &= \frac{1}{2}\mathbf{v}_j\mathbf{v}_i^T + \frac{1}{2}\mathbf{v}_i\mathbf{v}_j^T. \end{aligned}$$

Then we can get the following equation in the same fashion

$$c^{j,j}\mathbf{v}_j\mathbf{v}_j^T + c^{j,j-1}(\mathbf{v}_j\mathbf{v}_{j-1}^T + \mathbf{v}_{j-1}\mathbf{v}_j^T) + c^{j,j+1}(\mathbf{v}_j\mathbf{v}_{j+1}^T + \mathbf{v}_{j+1}\mathbf{v}_j^T) = \frac{1}{2}\mathbf{v}_j\mathbf{v}_i^T + \frac{1}{2}\mathbf{v}_i\mathbf{v}_j^T.$$

This proves that Eq. (A.3) holds.

Appendix B. Proof of the bounds on MVCs and their gradients

In Section 2.3, we have proposed the sufficient geometric constraints C1–C4 for polygonal domains in our application. In this section we prove that the MVCs and their gradients are uniformly bounded under the proposed geometric constraints C1–C4. Note that the geometric constraints for convex polygonal domains in this paper are slightly tighter than the constraints in [31], where the bounds of MVCs on convex polygonal domains have been proved. Hence, we only give brief proofs for the convex polygon case as it has already been covered in [31]. On the other hand, we provide detailed proofs for concave polygonal domains under our geometric constraints as a complement to the proofs in [31].

Now, let us consider the MVCs on a planar polygonal domain P as defined in Eqs. (1)–(2). Define $t_i(\mathbf{v}) = \tan(\alpha_i(\mathbf{v})/2)$ and $r_i(\mathbf{v}) = \|\mathbf{v}_i\mathbf{v}\|$ for all $\mathbf{v} \in P$. For simplicity, we omit the variable \mathbf{v} , then the gradients of MVCs can be written as

$$\nabla\phi_i = \frac{\nabla w_i \sum_{k=1}^n w_k - w_i \sum_{k=1}^n \nabla w_k}{(\sum_{k=1}^n w_k)^2} \quad \text{with} \quad \nabla w_i = \frac{\nabla t_{i-1} + \nabla t_i}{r_i} - \frac{t_{i-1} + t_i}{(r_i)^2} \nabla r_i. \quad (\text{B.1})$$

Following [31], we rewrite $\nabla\phi_i$ as the form

$$\nabla\phi_i = \frac{N_1 + N_2}{(\sum_{k=1}^n w_k)^2}, \quad (\text{B.2})$$

where

$$N_1 = \sum_{k=1}^n (t_{i-1} + t_i)(t_{k-1} + t_k) \left(\frac{\nabla r_k}{r_k^2 r_i} - \frac{\nabla r_i}{r_i^2 r_k} \right),$$

and

$$N_2 = \sum_{k=1}^n \frac{1}{r_i r_k} [(\nabla t_{i-1} + \nabla t_i)(t_{k-1} + t_k) - (t_{i-1} + t_i)(\nabla t_{k-1} + \nabla t_k)].$$

According to Theorem 4.1 in [31], both N_1 and N_2 in Eq. (B.2) can be expanded into sums of several terms in the following two forms

$$(t_{a-1} + t_a)(t_{b-1} + t_b) \frac{\nabla r_a}{r_a^2 r_b} \frac{1}{(\sum_{k=1}^n w_k)^2}, \quad a \neq b, \quad (\text{B.3})$$

and

$$\frac{\nabla t_i t_j}{r_a r_b} \frac{1}{(\sum_{k=1}^n w_k)^2}, \quad i \neq j, \quad a \neq b. \quad (\text{B.4})$$

Thus, to bound the gradients of MVCs, we only need to bound those two terms in Eqs. (B.3)–(B.4), respectively.

In the following discussion, we assume that the polygonal domain P for defining MVCs satisfies geometric constraints C1–C4 and $\text{diam}(P) = 1$. The bounds of MVCs and terms in Eqs. (B.3)–(B.4) will be proved in Theorems B.1–B.3, respectively. We will give a uniform constant to bound both MVCs and their gradients in Theorem B.4. Before we begin the proof of theorems, we introduce Lemmas B.1–B.11 as preparation. Proofs of Lemma B.3, Lemma B.5, Lemmas B.7 and B.8, which are independent of the angles of input polygons, are not provided as they can be found in [31]. The proofs of the other Lemmas use ideas similar to proofs of lemmas in Section 3 of [31]. In particular, Lemmas B.4, B.6 and B.9 are generalization of Proposition 3, Proposition 5 and Proposition 8 in [31] to the case where a concave vertex exists, respectively.

Lemma B.1. *If there exists $j \in \{1, \dots, n\}$, such that $\alpha_j(\mathbf{v}) < 0$, then $|\alpha_j(\mathbf{v})| < \pi - \beta$.*

Proof. Since $\alpha_j < 0$, P is concave. Assume \mathbf{v}_i is the only concave vertex of ∂P and \mathbf{p}_{i-1} (resp. \mathbf{p}_{i+1}) is the intersection of line $\mathbf{v}_{i-1}\mathbf{v}_i$ (resp. $\mathbf{v}_i\mathbf{v}_{i+1}$) and ∂P . The interior regions bounded by polygons $\{\mathbf{v}_{i+1}, \dots, \mathbf{p}_{i-1}, \mathbf{v}_i\}$ and $\{\mathbf{p}_{i+1}, \dots, \mathbf{v}_{i-1}, \mathbf{v}_i\}$ are denoted by R_1 and R_2 , respectively; see the gray regions in Fig. B.1(a&b). Angles $\alpha_i(\mathbf{v})$ (resp. $\alpha_{i-1}(\mathbf{v})$) become negative only when \mathbf{v} is in the region R_1 (resp. R_2). Let us consider the triangle $\Delta\mathbf{v}_{i-1}\mathbf{v}\mathbf{v}_i$,

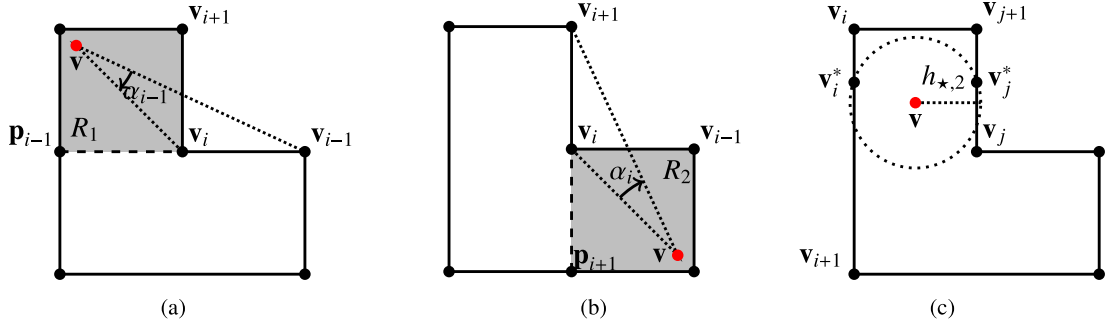


Fig. B.1. Notations for Lemmas B.1 and B.2.

where we have $|\alpha_{i-1}(\mathbf{v})| + |\angle(\mathbf{v}_{i-1}, \mathbf{v}_i, \mathbf{v}_{i+1})| < \pi$. Following the geometric constraint C2, we have

$$|\alpha_{i-1}(\mathbf{v})| < \pi - |\angle(\mathbf{v}_{i-1}, \mathbf{v}_i, \mathbf{v}_{i+1})| < \pi - \beta.$$

Similarly, we have $\alpha_i(\mathbf{v}) < 0$ and $|\alpha_i(\mathbf{v})| < \pi - \beta$ with \mathbf{v} in the region R_2 . \square

Lemma B.1 indicates a simple fact that there is at most one negative angle among $\alpha_1(\mathbf{v}), \dots, \alpha_n(\mathbf{v})$ under our geometric constraints C2 and C3, and the absolute value of the negative angle can be bounded by a constant less than π .

Lemma B.2. *There exists an $h_\star > 0$, such that for all $\mathbf{v} \in P$, $B(\mathbf{v}, h_\star)$ does not simultaneously intersect any three edges or any two non-adjacent edges of ∂P , where $B(\mathbf{v}, h_\star)$ denotes the circle with center point \mathbf{v} and radius h_\star .*

Proof. We first consider the case when P is convex. The existence of h_\star for convex domain has been proved in Proposition 9 of [35]. Together with geometric constraint C1.A, we choose

$$h_{\star,1} = \frac{d}{2\gamma^*(1+d)},$$

such that $B(\mathbf{v}, h_{\star,1})$ does not simultaneously intersect any three edges or any two non-adjacent edges of ∂P . In other words, $h_{\star,1}$ is chosen such that $B(\mathbf{v}, h_{\star,1})$ does not simultaneously intersect three edges of ∂P when P is a triangle ($n = 3$) or any two non-adjacent edges of ∂P when $n > 3$. Second, let us consider the case when P is concave, we use the proof by contradiction. Assume there exist a $\mathbf{v} \in P$ and an $h_{\star,2}$ such that $B(\mathbf{v}, h_{\star,2})$ intersects at least two non-adjacent edges $\mathbf{v}_i \mathbf{v}_{i+1}$ and $\mathbf{v}_j \mathbf{v}_{j+1}$; see Fig. B.1(c). Then, there exist $\mathbf{v}_i^* \in \mathbf{v}_i \mathbf{v}_{i+1}$, $\mathbf{v}_j^* \in \mathbf{v}_j \mathbf{v}_{j+1}$, such that $\mathbf{v}_i^*, \mathbf{v}_j^* \in B(\mathbf{v}, h_{\star,2})$. Moreover, following the geometric constraint C1.B, we have

$$d \leq \|\mathbf{v}_i^* \mathbf{v}_j^*\| \leq 2h_{\star,2}.$$

To ensure that $B(\mathbf{v}, h_{\star,2})$ does not intersect at least two non-adjacent edges of ∂P , we need to choose an $h_{\star,2}$, satisfying $0 < h_{\star,2} < d/2$. We have many choices of $h_{\star,2}$, such as $h_{\star,2} = d/4$. Note that $d \leq \text{diam}(P) = 1$ and $\sin \beta \leq 1$. To ease the discussion in Lemma B.6 (Inequality (B.5)), we choose a sufficiently small $h_{\star,2}$ such that

$$h_{\star,2} = \frac{d^2 \sin \beta}{4} < \frac{d}{2}.$$

To sum up, $h_\star = \min\{h_{\star,1}, h_{\star,2}\}$ satisfies all cases. \square

Lemma B.2 indicates that we have a constant h_\star for any vertex \mathbf{v} in P , such that $B(\mathbf{v}, h_\star)$ intersects ∂P at most a pair of adjacent edges of ∂P or only one edge. The geometric constraint C1 is sufficient for obtaining Lemma B.2.

Lemma B.3 (Corollary 3.2 in [31]). *If $r_i(\mathbf{v}) < h_\star$, then for all $j \neq i$, $r_j(\mathbf{v}) \geq h_\star$.*

Lemma B.4. *If $\alpha_i(\mathbf{v}) > \alpha_\star$, then $|\alpha_j(\mathbf{v})| < \alpha_\star$, for all $j \neq i$, where $\alpha_\star = \max\{\pi - \beta/2, 2 \arctan(1/h_\star)\}$.*

Proof. It has been proved in [31] that $\alpha_j(\mathbf{v}) < \alpha_\star$ when $\alpha_j \geq 0$. By Lemma B.1, we have

$$|\alpha_j| < \pi - \beta < \pi - \frac{\beta}{2} < \alpha_\star \quad \text{for } \alpha_j < 0. \quad \square$$

Lemma B.4 implies that there is at most one angle $\alpha_i(\mathbf{v})$ larger than α_\star .

Lemma B.5 (Proposition 3.4 in [31]). If $\alpha_i(\mathbf{v}) > \alpha_\star$, $r_j(\mathbf{v}) < h_\star$, then $j \in \{i, i+1\}$.

Lemma B.6. If $r_i(\mathbf{v}) < h_\star$, then $\alpha_{i-1}(\mathbf{v}) + \alpha_i(\mathbf{v}) > \min \{2\pi/3, 2\beta/3, \arcsin k_0\}$, where $k_0 = d(d^2 \sin \beta - h_\star)$. Moreover, $t_{i-1}(\mathbf{v}) + t_i(\mathbf{v}) \geq k_1$, where $k_1 = \min \{\sqrt{3}/2, \sin(\beta/3), k_0/2\}$.

Proof. We consider whether \mathbf{v}_i is concave or convex. If \mathbf{v}_i is a convex vertex, the result has been proved in [31], that is $\alpha_{i-1} + \alpha_i > 2\pi/3$. Otherwise, we define $\eta_i = |\angle(\mathbf{v}, \mathbf{v}_{i-1}, \mathbf{v}_i)|$ and $\zeta_i = |\angle(\mathbf{v}, \mathbf{v}_{i+1}, \mathbf{v}_i)|$; see Fig. B.2. Then we consider whether there exist negative angles between α_{i-1} and α_i .

Case 1: $\alpha_{i-1} \geq 0$, $\alpha_i \geq 0$. If $\alpha_{i-1}, \alpha_i > 0$, we sum up all the inner angles of $\triangle \mathbf{v}_i \mathbf{v} \mathbf{v}_{i+1}$ and $\triangle \mathbf{v}_{i-1} \mathbf{v} \mathbf{v}_i$; see Fig. B.2(a). Together with geometric constraint C2, we have

$$\alpha_{i-1} + \alpha_i + \eta_i + \zeta_i = |\angle(\mathbf{v}_{i-1}, \mathbf{v}_i, \mathbf{v}_{i+1})| > \beta.$$

Similar to [31], we can get $\eta_i < \frac{\alpha_{i-1}}{2}$, $\zeta_i < \frac{\alpha_i}{2}$. Then, we have

$$\alpha_{i-1} + \alpha_i > \frac{2}{3}\beta.$$

Otherwise, since $\mathbf{v} \in P$, only one of α_{i-1} and α_i can be zero at a time. Without loss of generality, we assume that $\alpha_{i-1} = 0$. Then, we only sum up all the inner angles of $\triangle \mathbf{v}_i \mathbf{v} \mathbf{v}_{i+1}$. Analogously, we have $\alpha_i + \zeta_i = |\angle(\mathbf{v}_{i-1}, \mathbf{v}_i, \mathbf{v}_{i+1})| > \beta$ and $\zeta_i < \frac{\alpha_i}{2}$, i.e., $\alpha_{i-1} + \alpha_i = \alpha_i > \frac{2}{3}\beta$.

Case 2: $\alpha_{i-1} < 0$ or $\alpha_i < 0$; see Fig. B.2(b). Without loss of generality, we suppose that $\alpha_{i-1} > 0$ and $\alpha_i < 0$. The area of $\triangle \mathbf{v}_{i-1} \mathbf{v}_i \mathbf{v}_{i+1}$ can be calculated by

$$S_{\triangle \mathbf{v}_{i-1} \mathbf{v}_i \mathbf{v}_{i+1}} = \frac{1}{2} \text{dist}(\mathbf{v}_i, \mathbf{v}_{i+1} \mathbf{v}_{i-1}) \|\mathbf{v}_{i+1} \mathbf{v}_{i-1}\| = \frac{1}{2} \|\mathbf{v}_{i-1} \mathbf{v}_i\| \|\mathbf{v}_i \mathbf{v}_{i+1}\| \sin |\angle(\mathbf{v}_{i-1}, \mathbf{v}_i, \mathbf{v}_{i+1})|,$$

where

$$\text{dist}(\mathbf{v}_i, \mathbf{v}_{i+1} \mathbf{v}_{i-1}) = \min_{\mathbf{v} \in [\mathbf{v}_{i+1} \mathbf{v}_{i-1}]} \|\mathbf{v} \mathbf{v}_i\|$$

is the shortest distance from \mathbf{v}_i to any point on line segment $\mathbf{v}_{i+1} \mathbf{v}_{i-1}$. By following Lemma B.2, we have

$$\text{dist}(\mathbf{v}_i, \mathbf{v}_{i+1} \mathbf{v}_{i-1}) = \frac{\|\mathbf{v}_{i-1} \mathbf{v}_i\| \|\mathbf{v}_i \mathbf{v}_{i+1}\| \sin |\angle(\mathbf{v}_{i-1}, \mathbf{v}_i, \mathbf{v}_{i+1})|}{\|\mathbf{v}_{i+1} \mathbf{v}_{i-1}\|} > d^2 \sin \beta > h_\star > r_i(\mathbf{v}) = \|\mathbf{v}_i \mathbf{v}\|. \quad (\text{B.5})$$

Since $\|\mathbf{v}_i \mathbf{v}\| < \text{dist}(\mathbf{v}_i, \mathbf{v}_{i+1} \mathbf{v}_{i-1})$, \mathbf{v} can only locate at one side of the line $\mathbf{v}_{i-1} \mathbf{v}_{i+1}$. Thus, we can get $\alpha_{i-1} + \alpha_i > 0$. By following the geometric assumption $\text{diam}(P) \leq 1$, we have

$$\sin(\alpha_{i-1} + \alpha_i) = \frac{\text{dist}(\mathbf{v}, \mathbf{v}_{i+1} \mathbf{v}_{i-1}) \|\mathbf{v}_{i+1} \mathbf{v}_{i-1}\|}{\|\mathbf{v} \mathbf{v}_{i+1}\| \|\mathbf{v} \mathbf{v}_{i-1}\|} \geq d(\text{dist}(\mathbf{v}_i, \mathbf{v}_{i+1} \mathbf{v}_{i-1}) - h_\star). \quad (\text{B.6})$$

Applying $\text{dist}(\mathbf{v}_i, \mathbf{v}_{i+1} \mathbf{v}_{i-1}) > d^2 \sin \beta$ in Inequality (B.5) to Inequality (B.6), we have

$$\alpha_{i-1} + \alpha_i > \arcsin k_0 > 0,$$

where $k_0 = d(d^2 \sin \beta - h_\star) > 0$. Define $k_1 = \min \{\sqrt{3}/2, \sin(\beta/3), k_0/2\}$. If $r_i(\mathbf{v}) < h_\star$, then the following inequality holds

$$t_{i-1} + t_i = \tan \frac{\alpha_{i-1}}{2} + \tan \frac{\alpha_i}{2} = \frac{\sin(\frac{\alpha_{i-1} + \alpha_i}{2})}{\cos \frac{\alpha_{i-1}}{2} \cos \frac{\alpha_i}{2}} \geq \sin(\frac{\alpha_{i-1} + \alpha_i}{2}) \geq k_1. \quad \square$$

Lemma B.7 (Proposition 3.6 in [31]). $|\nabla \alpha_i(\mathbf{v})| \leq 1/r_i(\mathbf{v}) + 1/r_{i+1}(\mathbf{v})$.

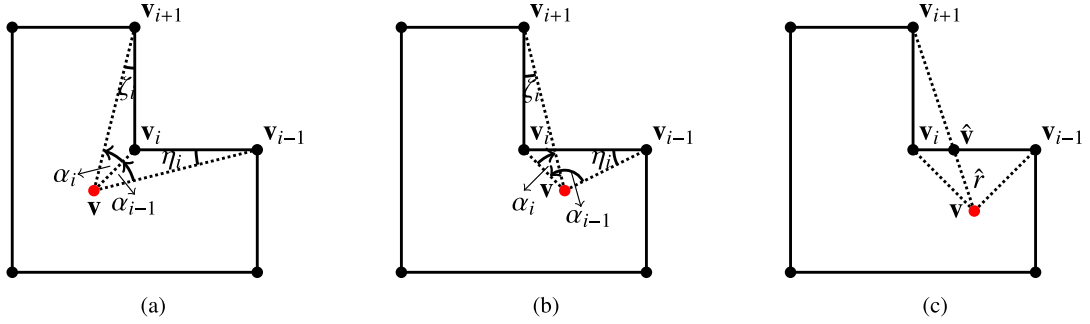


Fig. B.2. Notations for Lemmas B.6 and B.9.

Lemma B.8 (Proposition 3.7 in [31]). $\nabla r_i(\mathbf{v}) = (\mathbf{v} - \mathbf{v}_i) / \|\mathbf{v} - \mathbf{v}_i\|$, and $|\nabla r_i(\mathbf{v})| = 1$.

Lemma B.9.

$$\sum_{k=1}^n w_k(\mathbf{v}) > 2\pi. \quad (\text{B.7})$$

Proof. The case of convex P has been proved in [31]. Here we only need to consider the case where P is concave.

If all $\alpha_i(\mathbf{v}) \geq 0$, we can obtain Inequality (B.7) in the same fashion as done in [31]. Since there is at most one concave vertex \mathbf{v}_i of ∂P , we suppose that $\alpha_i(\mathbf{v}) < 0$ without loss of generality. Let $\hat{\mathbf{v}}$ be the intersection of segments $\mathbf{v}_{i-1}\mathbf{v}$ and $\mathbf{v}_i\mathbf{v}_{i+1}$; see Fig. B.2(c). Then, the intersection point can be represented as $\hat{\mathbf{v}} = (1 - \mu)\mathbf{v}_{i-1} + \mu\mathbf{v}_i$, $0 < \mu < 1$. We refine P to \hat{P} by introducing the point $\hat{\mathbf{v}}$ between \mathbf{v}_{i-1} and \mathbf{v}_i , and denote the weight functions with respect to \hat{P} as defined in Eq. (1) by $\hat{w}_1, \dots, \hat{w}_n$ and \hat{w} . Thus, we have $w_{i-1} = \hat{w}_{i-1} + (1 - \mu)\hat{w}$, $w_i = \hat{w}_i + \mu\hat{w}$, $w_k = \hat{w}_k$ for $k \neq i - 1, i$. Let $u_k = (1/r_k + 1/r_{k+1}) \tan(\alpha_k/2)$, $\hat{\alpha} = -\alpha_i$, and $\hat{r} = \|\mathbf{v}\hat{\mathbf{v}}\|$, then we have

$$\alpha_{i-1} = \hat{\alpha}_{i-1} + \hat{\alpha}, \quad \alpha_i = -\hat{\alpha}, \quad \alpha_k = \hat{\alpha}_k, \quad k \neq i - 1, i;$$

$$\hat{u}_{i-1} = \left(\frac{1}{r_{i-1}} + \frac{1}{\hat{r}}\right) \tan \frac{\hat{\alpha}_{i-1}}{2}, \quad \hat{u}_i = \left(\frac{1}{r_i} + \frac{1}{\hat{r}}\right) \tan \frac{\hat{\alpha}}{2}, \quad u_k = \hat{u}_k, \quad k \neq i - 1.$$

Since $\hat{r} < r_{i+1}$, $\hat{u} + \hat{u}_i > 0$, and $\text{diam}(P) = \text{diam}(\hat{P}) = 1$, we have

$$\sum_{k=1}^n w_k = \sum_{k=1}^n \hat{w}_k + \hat{w} = \sum_{k=1}^n \hat{u}_k + \hat{u} > \sum_{k \neq i} \hat{u}_k = \sum_{k \neq i-1, i} \hat{u}_k + \hat{u}_{i-1} > \sum_{k \neq i-1, i} \alpha_k + \hat{\alpha}_{i-1} = \sum_{k=1}^n \alpha_k = 2\pi. \quad \square$$

It is worth pointing out that the geometric constraint C3 is not necessary for this lemma. For polygonal domain with more than one concave vertex, the negative terms in the left side of Inequality (B.7) cannot be canceled out by adding a single intersection point. In this case, Inequality (B.7) can still be obtained by introducing more intersection points of the line segment $\mathbf{v}\mathbf{v}_i$ and the edges of ∂P in the same fashion as [48].

Lemma B.10. If $r_a(\mathbf{v}) < h_*$, there exists a constant $L_1 > 0$, such that for all $a \neq b$,

$$|t_{b-1}(\mathbf{v}) + t_b(\mathbf{v})| < L_1 |t_{a-1}(\mathbf{v}) + t_a(\mathbf{v})|. \quad (\text{B.8})$$

Proof. By Lemmas B.4–B.5, we have

$$\min \{|\alpha_{a-1}|, |\alpha_a|\} \leq \alpha_* \text{ and } |\alpha_i| \leq \alpha_*, \quad \forall i \neq a - 1, a. \quad (\text{B.9})$$

Following Inequality (B.9), we have that there exists at most one angle larger than α_* between α_{a-1} and α_a . The following discussion is based on whether α_{b-1} or α_b is larger than α_* .

Case 1: $\alpha_{b-1} > \alpha_*$ or $\alpha_b > \alpha_*$. Without loss of generality, we suppose that $\alpha_b > \alpha_*$. Since $a \neq b$ and $\alpha_b > \alpha_*$, we have $b = a - 1$, i.e., $\alpha_b = \alpha_{a-1} > \alpha_*$. By Lemma B.1, for all $i \in \{1, 2, \dots, n\}$, there exists at most one negative angle among α_i . We consider the subcases of $\alpha_a \geq 0$ and $\alpha_a < 0$ as follows:

- $\alpha_a \geq 0$. By two conclusions in Inequality (B.9) and $t_a \geq 0$, we have

$$|t_{b-1} + t_b| \leq 2t_b = 2t_{a-1} \leq 2(t_{a-1} + t_a).$$

- $\alpha_a < 0$. Define $x = t_b = t_{a-1}$, $y = t_{b-1}$, $z = t_a$, $a_0 = \tan \frac{\pi-\beta}{2}$, and $b_0 = \tan \frac{\alpha_*}{2}$. Note that $x \in (b_0, +\infty)$ and $0 < a_0 < b_0$. By Lemma B.1, we get $|\alpha_a| < \pi - \beta$, thus we have $z \in (-a_0, 0)$. By those two conclusions in Inequality (B.9), we have $y \in [0, b_0)$. The inequality to prove becomes: $(x+y) \leq L_1(x+z)$, i.e., $L_1 \geq \frac{x+y}{x+z}$. Define $g_1(x) = \frac{x+b_0}{x-a_0}$ and set $L_1 = g_1(b_0)$, then we have $L_1 > g_1(x) > \frac{x+y}{x+z}$, i.e.,

$$|t_{b-1} + t_b| \leq g_1(b_0)|t_{a-1} + t_a|.$$

Case 2: $\alpha_{b-1} \leq \alpha_*$, $\alpha_b \leq \alpha_*$. By Lemma B.6, there exists $k_1 > 0$, such that $t_{a-1} + t_a \geq k_1$, then we have

$$|t_{b-1} + t_b| \leq \frac{2 \tan \frac{\alpha_*}{2}}{k_1} |t_{a-1} + t_a|. \quad \square$$

Lemma B.11. If $\alpha_b(\mathbf{v}) > \alpha_*$, $b \in \{a-1, a\}$, there exists a constant $L_2 > 0$, such that

$$t_b(\mathbf{v}) \leq L_2 |t_{a-1}(\mathbf{v}) + t_a(\mathbf{v})|.$$

Proof. By Lemma B.1, there exists at most one negative angle among α_i . Note that, $b \in \{a-1, a\}$. Without loss of generality, we suppose $b = a-1$. The following discussion is based on whether α_{a-1} or α_a is negative. If both α_{a-1} and α_a are non-negative, we can simply set $L_2 = 1$. Thus, we have

$$t_b = t_{a-1} \leq L_2 |t_{a-1} + t_a| = |t_{a-1} + t_a|.$$

Otherwise, we define $x = t_b = t_{a-1}$, $z = t_a$, $b_0 = \tan \frac{\alpha_*}{2}$ and $a_0 = \tan \frac{\pi-\beta}{2}$. We have already observed that $x \in (b_0, +\infty)$ and $0 < a_0 < b_0$. By Lemma B.1, we have $z \in (-a_0, 0)$. By Lemma B.6, we have $t_{a-1} + t_a > 0$. The inequality to prove becomes: $x \leq L_2(x+z)$, i.e., $L_2 \geq \frac{x}{x+z}$. Define $g_2(x) = \frac{x}{x-a_0}$ and set $L_2 = g_2(b_0)$. Then, we have $L_2 > g_2(x) > \frac{x}{x+z}$, i.e.,

$$t_b \leq g_2(b_0) |t_{a-1} + t_a|. \quad \square$$

The geometric constraint C3 ensures that the negative angles can be bounded by α_* . If we remove the geometric constraint C3, there may exist negative angles smaller than $-\alpha_*$, thus Lemmas B.3, B.10 and B.11 will no longer hold. We can now give the main theorems.

Theorem B.1. For all $\mathbf{v} \in P$, there exists a uniform constant $M_0 > 0$, such that

$$|\phi_i(\mathbf{v})| \leq M_0, \quad |w_i(\mathbf{v})| \leq M_0 \left(\sum_{k=1}^n w_k(\mathbf{v}) \right), \quad i \in \{1, 2, \dots, n\}. \quad (\text{B.10})$$

Proof. According to Lemma B.1, there exists at most one negative angle among α_k . Hence, there are at most two negative weight functions w_k in the right side of Inequality (B.10). For each $i \in \{1, \dots, n\}$, we divide the situation into two cases depending on whether there are any negative terms among w_k or not.

Case 1: $w_k \geq 0$ for $k \in \{1, 2, \dots, n\}$. By the definition of MVCs, we have

$$0 \leq \phi_i \leq 1.$$

Case 2: $\exists a \in \{1, 2, \dots, n\}$, $w_a < 0$ or $w_{a+1} < 0$, and $w_j > 0$ for $j \neq a, a+1$. We further break the proof into two subcases depending on whether w_i is larger than zero or not.

Case 2.1: If $w_i < 0$, we have $\alpha_{i-1} + \alpha_i < 0$. By Lemma B.6, we have $r_i \geq h_*$. Note that there is at most one negative angle. Without loss of generality, we assume that $\alpha_{i-1} \geq 0$ and $\alpha_i < 0$. Then, we have $\alpha_{i-1} < |\alpha_i|$. By Lemma B.1, we have $\alpha_{i-1} < |\alpha_i| < \pi - \beta$. By Lemma B.9, we have $\sum_{k=1}^n w_k > 2\pi$. Thus we have

$$|\phi_i| = \frac{t_{i-1} + t_i}{r_i} \frac{1}{\sum_{k=1}^n w_k} \leq \frac{\tan \frac{\pi-\beta}{2}}{h_* \pi}.$$

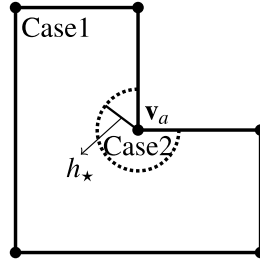


Fig. B.3. Different cases for [Theorem B.2](#).

Case 2.2: If $w_i \geq 0$, we rewrite ϕ_i as the form $\phi_i = \frac{w_i}{w_i + \sum_{k \neq i} w_k}$. If $\sum_{k \neq i} w_k \geq 0$, we have $0 \leq \phi_i \leq 1$. Otherwise, there exist at most two consecutive terms that are negative among w_k , with $k \neq i$. Without loss of generality, we suppose that $w_b < 0$ and $w_{b+1} < 0$, where $b \neq i-1, i$. Then we have $\alpha_{b-1} + \alpha_b < 0$ and $\alpha_b + \alpha_{b+1} < 0$. By [Lemma B.6](#), we have $r_b \geq h_*$ and $r_{b+1} \geq h_*$. Since there exists at most one negative angle among α_k , we have $\alpha_b < 0$, $\alpha_{b-1} \geq 0$, and $\alpha_{b+1} \geq 0$. Since $\sum_{k \neq i} w_k < 0$, we have $\sum_{k \neq i, b, b+1} w_k < |w_b + w_{b+1}|$. By [Lemma B.1](#), we have $\alpha_{b-1}, |\alpha_b|, \alpha_{b+1} < \pi - \beta$. Thus we have

$$\left| \sum_{k \neq i} w_k \right| \leq 2|w_b + w_{b+1}| \leq 8 \frac{\tan \frac{\pi - \beta}{2}}{h_*}.$$

By [Lemma B.9](#), we have $\sum_k w_k > 2\pi$. Hence ϕ_i can be bounded as follows

$$|\phi_i| = \left| 1 - \frac{\sum_{k \neq i} w_k}{\sum_k w_k} \right| \leq 1 + \frac{|\sum_{k \neq i} w_k|}{2\pi} \leq 1 + 4 \frac{\tan \frac{\pi - \beta}{2}}{h_* \pi}.$$

To sum up, $\phi_i, i \in \{1, \dots, n\}$ are uniformly bounded by $M_0 = 1 + 4 \frac{\tan \frac{\pi - \beta}{2}}{h_* \pi}$ in all cases. Since $\sum_{k=1}^n w_k > 2\pi$ ([Lemma B.9](#)), we have $|w_i| \leq M_0(\sum_{k=1}^n w_k)$ for all $i \in \{1, 2, \dots, n\}$. \square

In [Theorem B.1](#), we give a uniform constant to bound all the MVCs under our geometric constraints. According to [48], $\phi_i(\mathbf{v})$ is a continuous function, hence can be bounded on the bounded closed set \bar{P} . Therefore, we believe that MVCs can be bounded subjected to more relaxed geometric constraints, however, the uniform bounds may be given in other ways.

Theorem B.2. For all $\mathbf{v} \in P$ and $a \neq b$, there exists a uniform constant $C_1 > 0$, such that

$$|(t_{a-1}(\mathbf{v}) + t_a(\mathbf{v}))(t_{b-1}(\mathbf{v}) + t_b(\mathbf{v})) \frac{\nabla r_a(\mathbf{v})}{r_a^2(\mathbf{v}) r_b(\mathbf{v})}| \leq C_1 \left(\sum_{k=1}^n w_k(\mathbf{v}) \right)^2.$$

Proof. The proof is essentially the same as the proof of Lemma 4.2 in [31], except that we now have to deal with concave polygonal domains. Besides, our proof is more succinct than the one given in [31] by applying [Lemma B.10](#).

By the geometry assumption of $\text{diam}(P) = 1$ and [Lemma B.7](#), we have $r_i \leq 1$ and $|\nabla r_i| = 1$ for $i \in \{1, \dots, n\}$. By [Lemma B.3](#), we have $\max\{r_a, r_b\} \geq h_*$. Without loss of generality, we suppose $r_b \leq r_a$ and consider the cases whether r_a is larger than h_* or not. We give an illustration for two cases when v_a is a concave vertex; see [Fig. B.3](#).

Case 1: $r_a \geq h_*$. By Inequality (B.10), we have

$$|(t_{a-1} + t_a)(t_{b-1} + t_b) \frac{\nabla r_a}{r_a^2 r_b}| = |w_a w_b \frac{\nabla r_a}{r_a}| \leq |w_a| |w_b| \frac{1}{r_a} \leq M_0^2 \frac{1}{h_*} \left(\sum_{k=1}^n w_k \right)^2.$$

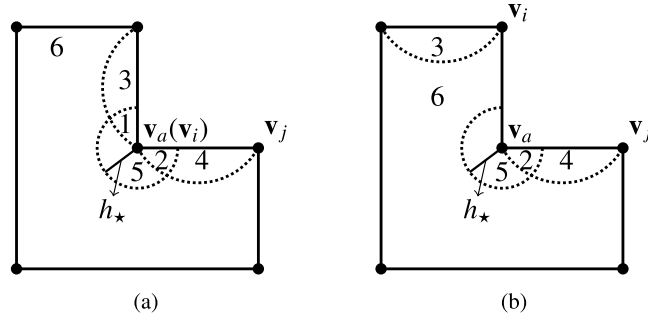


Fig. B.4. Different cases for Theorem B.3. (a) $i = a$; (b) $i, j \neq a$.

Case 2: $r_a < h_*$. By Lemma B.3, we have $r_b \geq h_*$. By Lemma B.10, there exists $L_1 > 0$, such that $|t_{b-1} + t_b| \leq L_1|t_{a-1} + t_a|$, thus we have

$$|(t_{a-1} + t_a)(t_{b-1} + t_b) \frac{\nabla r_a}{r_a^2 r_b}| \leq L_1 \frac{(t_{a-1} + t_a)^2}{r_a^2} \frac{|\nabla r_a|}{r_b} \leq L_1 \frac{1}{h_*} w_a^2 \leq L_1 M_0^2 \frac{1}{h_*} \left(\sum_{k=1}^n w_k \right)^2. \quad \square$$

Theorem B.3. For all $\mathbf{v} \in P$ and $i \neq j$, $a \neq b$, there exists a uniform constant $C_2 > 0$, such that

$$\left| \frac{\nabla t_i(\mathbf{v}) t_j(\mathbf{v})}{r_a(\mathbf{v}) r_b(\mathbf{v})} \right| \leq C_2 \left(\sum_{k=1}^n w_k(\mathbf{v}) \right)^2.$$

Proof. We also generalize the idea of proof of Lemma 4.3 in [31] to both convex and concave polygonal domains. In particular, we bound $t_b(\mathbf{v})$ when $\alpha_b(\mathbf{v}) > \alpha_*$, $b \in \{a-1, a\}$ by using Lemma B.11, instead of using the trivial inequality $t_b(\mathbf{v}) < t_{a-1}(\mathbf{v}) + t_a(\mathbf{v})$ in convex polygonal domains. By Lemma B.7, we have

$$|\nabla t_i| \leq \frac{1}{2 \cos^2 \frac{\alpha_i}{2}} \left(\frac{1}{r_i} + \frac{1}{r_{i+1}} \right). \quad (\text{B.11})$$

By Lemma B.3, we have $\max \{r_a, r_b\} \geq h_*$. Without loss of generality, we suppose that $r_a \leq r_b$, and $r_b \geq h_*$. By Lemma B.4, we have $\min \{|\alpha_i|, |\alpha_j|\} \leq \alpha_*$ and $\alpha_* > \frac{\pi}{2}$. Define m the subscript of the minimum between r_i and r_{i+1} . We consider the cases whether there exists an angle larger than α_* between α_i and α_j and whether r_a is larger than h_* or not. We give an illustration for two cases when v_a is a concave vertex; see Fig. B.4.

Case 1: $\alpha_i > \alpha_*$, $r_a < h_*$. Note that $|\alpha_j| \leq \alpha_*$ and $r_b \geq h_*$, we have

$$\left| \frac{t_j}{r_b} \right| < \frac{\tan \frac{\alpha_*}{2}}{h_*}. \quad (\text{B.12})$$

As $\pi > \alpha_i > \alpha_* > \frac{\pi}{2}$, we have $1 < 2 \sin^2 \frac{\alpha_i}{2}$. Following Eq. (B.11), we have

$$|\nabla t_i| \leq \frac{1}{2 \cos^2 \frac{\alpha_i}{2}} \left(\frac{1}{r_i} + \frac{1}{r_{i+1}} \right) \leq \frac{\sin^2 \frac{\alpha_i}{2}}{\cos^2 \frac{\alpha_i}{2}} \frac{2}{r_a} \leq 2 \frac{t_i^2}{r_a}.$$

By Lemma B.5, we have $a \in \{i, i+1\}$. By Inequality (B.10) and Lemma B.11, the following inequality holds,

$$|\nabla t_i| \leq 2L_2^2 \frac{(t_a + t_{a-1})^2}{r_a} = 2L_2^2 w_a^2 r_a \leq 2L_2^2 M_0^2 \left(\sum_{k=1}^n w_k \right)^2 r_a. \quad (\text{B.13})$$

Finally, we integrate Inequalities (B.12) and (B.13) together and have

$$\left| \frac{\nabla t_i t_j}{r_a r_b} \right| \leq 2L_2^2 M_0^2 \frac{\tan \frac{\alpha_*}{2}}{h_*} \left(\sum_{k=1}^n w_k \right)^2.$$

Case 2: $\alpha_j > \alpha_*$, $r_a < h_*$. Note that $r_b \geq h_*$, $|\alpha_i| \leq \alpha_*$, we have $0 \leq |\alpha_i| \leq \alpha_* < \pi$, $\cos \frac{\alpha_i}{2} > \cos \frac{\alpha_*}{2}$. By Eq. (B.11), we have

$$|\nabla t_i| \leq \frac{1}{2 \cos^2 \frac{\alpha_*}{2}} \frac{2}{r_a}.$$

Since $\alpha_* > \frac{\pi}{2}$, we have $t_j > \tan \frac{\alpha_*}{2} > 1$. By Lemma B.5, we have $j \in \{a, a-1\}$. By Lemma B.11, we have $t_j < t_j^2 < L_2^2(t_{a-1} + t_a)^2 = L_2^2 w_a^2 r_a^2$. Thus, we have

$$\left| \frac{\nabla t_i t_j}{r_a r_b} \right| < \frac{L_2^2}{\cos^2 \frac{\alpha_*}{2} h_*} w_a^2 \leq \frac{L_2^2 M_0^2}{\cos^2 \frac{\alpha_*}{2} h_*} \left(\sum_{k=1}^n w_k \right)^2.$$

Case 3: $\alpha_i > \alpha_*$, $r_a \geq h_*$. By defining $r_m = \min \{r_i, r_{i+1}\}$, we have

$$\left| \frac{\nabla t_i t_j}{r_a r_b} \right| \leq \frac{\tan \frac{\alpha_*}{2}}{h_*^2} t_i^2 \frac{2}{r_m}.$$

Following Inequality (B.10) and Lemma B.11, since $r_m < \text{diam}(P) = 1$, we have

$$\frac{t_i^2}{r_m} \leq L_2^2 \frac{(t_m + t_{m-1})^2}{r_m^2} \leq L_2^2 w_m^2 \leq L_2^2 M_0^2 \left(\sum_{k=1}^n w_k \right)^2.$$

Thus, we have

$$\left| \frac{\nabla t_i t_j}{r_a r_b} \right| < \frac{2 \tan \frac{\alpha_*}{2}}{h_*^2} L_2^2 M_0^2 \left(\sum_{k=1}^n w_k \right)^2.$$

Case 4: $\alpha_j > \alpha_*$, $r_a \geq h_*$. We obtain

$$\left| \frac{\nabla t_i t_j}{r_a r_b} \right| \leq \frac{t_j}{\cos^2 \frac{\alpha_*}{2} h_*^2 r_m} \frac{1}{r_m},$$

and split the proof of this case into two subcases as follows.

Case 4.1: $r_m \geq h_*$. Note that $\alpha_j > \alpha_*$, $t_j > 1$. By Lemma B.11, we have $t_j < t_j^2 < L_2^2 w_j^2 r_j^2 < L_2^2 w_j^2 < L_2^2 M_0^2 \left(\sum_{k=1}^n w_k \right)^2$. Thus, we have

$$\left| \frac{\nabla t_i t_j}{r_a r_b} \right| \leq \frac{L_2^2 M_0^2}{\cos^2 \frac{\alpha_*}{2} h_*^3} \left(\sum_{j=1}^n w_j \right)^2.$$

Case 4.2: $r_m < h_*$. By Lemma B.5, we have $m \in \{j, j+1\}$. By Lemma B.11, we have $t_j < L_2^2 w_m^2 r_m^2 < L_2^2 w_m^2 r_m < L_2^2 M_0^2 r_m \left(\sum_{k=1}^n w_k \right)^2$. Thus, we have

$$\left| \frac{\nabla t_i t_j}{r_a r_b} \right| \leq \frac{L_2^2 M_0^2}{\cos^2 \frac{\alpha_*}{2} h_*^2} \left(\sum_{k=1}^n w_k \right)^2.$$

Case 5: $|\alpha_i| \leq \alpha_*$, $|\alpha_j| \leq \alpha_*$, $r_a < h_*$. We obtain

$$\left| \frac{\nabla t_i t_j}{r_a r_b} \right| \leq \frac{\tan \frac{\alpha_*}{2}}{\cos^2 \frac{\alpha_*}{2} h_*} \frac{1}{r_a^2}.$$

By Lemma B.6 and $r_a < h_*$, there exists $k_1 > 0$ as defined in Lemma B.6, such that $t_{a-1} + t_a \geq k_1$. Then we have

$$\left| \frac{\nabla t_i t_j}{r_a r_b} \right| \leq \frac{\tan \frac{\alpha_*}{2}}{\cos^2 \frac{\alpha_*}{2} h_*} \frac{k_1^2}{k_1^2 r_a^2} \leq \frac{\tan \frac{\alpha_*}{2}}{\cos^2 \frac{\alpha_*}{2} h_* k_1^2} w_a^2 \leq \frac{\tan \frac{\alpha_*}{2} M_0^2}{\cos^2 \frac{\alpha_*}{2} h_* k_1^2} \left(\sum_{k=1}^n w_k \right)^2.$$

Case 6: $|\alpha_i| \leq \alpha_*$, $|\alpha_j| \leq \alpha_*$, $r_a \geq h_*$. We obtain

$$\left| \frac{\nabla t_i t_j}{r_a r_b} \right| \leq \frac{\tan \frac{\alpha_*}{2}}{\cos^2 \frac{\alpha_*}{2} h_*^2} \frac{1}{r_m}.$$

Case 6.1: $r_m \geq h_\star$. By Lemma B.9 and $\sum_{k=1}^n w_k > 2\pi$, we have

$$\left| \frac{\nabla t_i t_j}{r_a r_b} \right| \leq \frac{\tan \frac{\alpha_\star}{2} (2\pi)^2}{\cos^2 \frac{\alpha_\star}{2} h_\star^3 (2\pi)^2} \leq \frac{\tan \frac{\alpha_\star}{2}}{\cos^2 \frac{\alpha_\star}{2} h_\star^3 4\pi^2} \left(\sum_{k=1}^n w_k \right)^2.$$

Case 6.2: $r_m < h_\star$. By Lemma B.6 and $r_m^2 < r_m$, there exists $k_1 > 0$, such that $t_{m-1} + t_m \geq k_1$. Then, we have

$$\left| \frac{\nabla t_i t_j}{r_a r_b} \right| \leq \frac{\tan \frac{\alpha_\star}{2}}{\cos^2 \frac{\alpha_\star}{2} h_\star^2} \frac{k_1^2}{k_1^2 r_m} \leq \frac{\tan \frac{\alpha_\star}{2} M_0^2}{\cos^2 \frac{\alpha_\star}{2} h_\star^2 k_1^2} \left(\sum_{k=1}^n w_k \right)^2. \quad \square$$

Theorem B.4. For all $\mathbf{v} \in P$, there exists a uniform constant $C_g > 0$, such that

$$|\phi_i(\mathbf{v})| \leq C_g, \quad |\nabla \phi_i(\mathbf{v})| \leq C_g, \quad i \in \{1, 2, \dots, n\}.$$

Proof. We have given the bounds of terms in Eq. (B.3) and Eq. (B.4) in Theorem B.2 and Theorem B.3, respectively. Similar to Theorem 4.1 in [31], we find a constant $M_1 = 2C_1 n^\star + 8C_2 n^\star$ to bound $\nabla \phi_i$, such that

$$|\nabla \phi_i(\mathbf{v})| \leq M_1, \quad i \in \{1, 2, \dots, n\},$$

where n^\star is the maximum vertex count defined in geometric constraint C4, and C_1 and C_2 are constants given by Theorems B.2 and B.3, respectively. Together with the bound M_0 of MVCs in Theorem B.1, we set a uniform constant $C_g = \max \{M_0, M_1\}$ to bound MVCs and their gradients. \square

Appendix C. Proof of interpolation error estimates

This section proves the interpolation error estimates for QSE shape functions under geometric constraints C1–C4, based on the bounds on the MVCs and their gradients proved in Appendix B and the Bramble–Hilbert lemma [32]. Let us first introduce some notations and recall the Bramble–Hilbert lemma.

- (1) **Star-shaped domain [32]:** A polygonal domain Ω is star-shaped if there exists a ball $B \subset \Omega$ such that for each point $x \in \Omega$, the closed convex hull of $\{x\} \cup B$ belongs to Ω .
- (2) **Chunkiness parameter $\gamma(\Omega)$ of a star-shaped domain Ω [32]** $\gamma(\Omega) = \frac{\text{diam}(\Omega)}{\rho}$, where ρ is the radius of the largest ball $B \subset \Omega$ for Ω to be a star-shaped domain.

Lemma C.1 (Bramble–Hilbert Lemma [32]).: Let Ω be star-shaped and let $u \in H^3(\Omega)$, then there exist a quadratic polynomial $p(u)$ and a constant C_γ (depending on the chunkiness parameter $\gamma(\Omega)$) such that

$$|u - p(u)|_{H^k(\Omega)} \leq C_\gamma \text{diam}(\Omega)^{(3-k)} |u|_{H^3(\Omega)}, \quad k = 0, 1, 2, 3.$$

The following lemma shows that a polygonal domain P with the unit diameter satisfying geometric constraints C1–C4 is a star-shaped domain.

Lemma C.2. Let P be a polygonal domain with $\text{diam}(P) = 1$ and satisfying geometric constraints C1–C4, then P is star-shaped and the chunkiness parameter is bounded, i.e., there exists a constant γ_\star , such that $\gamma(P) \leq \gamma_\star$.

Proof. We first consider the case when P is concave and satisfies geometric constraints C1–C4. Assume that \mathbf{v}_i is the only concave vertex of ∂P and \mathbf{p}_{i-1} (resp. \mathbf{p}_{i+1}) is the intersection of line $\mathbf{v}_{i-1}\mathbf{v}_i$ (resp. $\mathbf{v}_i\mathbf{v}_{i+1}$) and ∂P . Then, vertices $\{\mathbf{v}_i, \mathbf{p}_{i-1}, \dots, \mathbf{p}_{i+1}\}$ form a convex polygon, denoted by K , see Fig. C.1. Assume B is the largest ball of radius ρ inscribed in polygon K . Note that line $\mathbf{v}_{i-1}\mathbf{p}_{i-1}$ (resp. $\mathbf{v}_{i+1}\mathbf{p}_{i+1}$) partitions the concave domain into two convex regions. For any given points $\mathbf{v} \in P$ and $\mathbf{b} \in B$, the polygonal domain P contains the whole line segment that joins them. In other words, P is star-shaped. We denote $\gamma_\star = \max\{\gamma^\star, \frac{2}{d}\}$, where γ^\star and d are defined in geometric constraint C1. Following geometric constraint C1.B, we have $2\rho \geq d$, and

$$\gamma(P) = \frac{\text{diam}(P)}{\rho} \leq \frac{2}{d} \leq \gamma_\star.$$

Now let us consider the case when P is convex. Assume B is the largest circle of radius ρ inscribed in P . By geometric constraint C1.A, we have $\gamma(P) \leq \gamma^\star \leq \gamma_\star$. \square

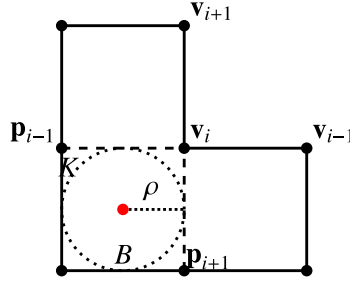


Fig. C.1. Notation for the largest ball B of radius ρ in a star-shaped polygonal domain.

Next, we prove the bound of the interpolation operator I on a polygonal domain P defined in Section 2.3, where we generalize the proof for a convex polygonal domain in Lemma 2 of [35] to concave polygonal domains satisfying geometric constraints C1–C4.

Lemma C.3. *Let P be a polygonal domain with $\text{diam}(P) = 1$ and satisfying geometric constraints C1–C4, and $u \in H^2(P)$, then there exists a constant C_i such that*

$$\|Iu\|_{H^1(P)} \leq C_i \|u\|_{H^2(P)}.$$

Proof. Note that the boundary ∂P satisfying geometric constraints C1–C4 is uniformly Lipschitz [33,35]. By Sobolev embedding theorem [33,34], there exists a constant C_s independent of the boundary ∂P , such that for all $u \in H^2(P)$, $\|u\|_{C^0(\bar{P})} \leq C_s \|u\|_{H^2(P)}$, where $\|u\|_{C^0(\bar{P})} = \max_{\mathbf{v} \in \bar{P}} u(\mathbf{v})$. Set $C_i = 2n^* C_q C_s$. Following Theorem 3 in Section 2.3 and Sobolev embedding theorem, we have

$$\|Iu\|_{H^1(P)} \leq \sum_{i=1}^{2n} |u(\mathbf{v}_i)| \|\psi_i\|_{H^1(P)} \leq 2n^* C_q \|u\|_{C^0(\bar{P})} \leq 2n^* C_q C_s \|u\|_{H^2(P)} \leq C_i \|u\|_{H^2(P)}. \quad \square$$

The following theorem shows the interpolation error estimates for the QSE shape functions on a polygonal domain with the unit diameter and satisfying geometric constraints C1–C4.

Theorem C.1. *Let P be a polygonal domain satisfying geometric constraints C1–C4 and with $\text{diam}(P) = 1$, then for all $u \in H^3(P)$, there exists a constant C_e such that*

$$\|u - Iu\|_{H^1(P)} \leq C_e |u|_{H^3(P)}.$$

Proof. Let $p(u)$ be the quadratic polynomial given in Lemma C.1. By following the quadratic precision of the QSE shape functions, we have $I p(u) = p(u)$. By Lemma C.1 and Lemma C.2, we have

$$|u - p(u)|_{H^k(P)} \leq C_\gamma |u|_{H^3(P)}, \quad k = 0, 1, 2, 3, \quad (\text{C.1})$$

where C_γ is a constant. Set $C_e = 2(1 + C_i)C_\gamma$. By following Inequality (C.1) and Lemma C.3, we have

$$\begin{aligned} \|u - Iu\|_{H^1(P)} &\leq \|u - p(u)\|_{H^1(P)} + \|I(u - p(u))\|_{H^1(P)} \leq (1 + C_i) \|u - p(u)\|_{H^2(P)} \\ &\leq (1 + C_i) \|u - p(u)\|_{H^3(P)} \leq 2(1 + C_i) C_\gamma |u|_{H^3(P)} \leq C_e |u|_{H^3(P)}. \quad \square \end{aligned}$$

Finally, we derive the interpolation error estimates for the QSE shape functions on any polygonal domain P satisfying geometric constraints C1–C4 by using uniform transformation [31]:

$$\mathcal{T} : R^2 \longrightarrow R^2, \mathcal{T}\mathbf{v} = \frac{1}{\text{diam}(P)} \mathbf{v}, \mathbf{v} \in R^2.$$

The image of P under the uniform transformation \mathcal{T} is a polygonal domain with the unit diameter, denoted by $\mathcal{T}P$ and referred to as the reference polygonal domain of P . We say that functions f and $f_{\mathcal{T}}$ are invariant [31] with

respect to domain P if for all $v \in P$, $f(v) = f_{\mathcal{T}}(\mathcal{T}v)$. Following Remark 2 of [31], we have:

$$|f|_{H_k(P)} = \frac{1}{\text{diam}(P)^{1-k}} |f_{\mathcal{T}}|_{H_k(\mathcal{T}P)}, \quad k = 1, 2, \dots \quad (\text{C.2})$$

Theorem C.2. *Let P be a polygonal domain satisfying geometric constraints C1–C4, then for all $u \in H^3(P)$, there exists a constant C_e such that*

$$\|u - Iu\|_{H^1(P)} \leq C_e \text{diam}(P)^2 |u|_{H^3(P)}.$$

Proof. For a given function $u \in H^3(P)$, we define a function $u_{\mathcal{T}}$ on $\mathcal{T}P$ as $u_{\mathcal{T}}(v) = u(\mathcal{T}^{-1}v)$ for $\forall v \in \mathcal{T}P$, where $\mathcal{T}^{-1}v = \text{diam}(P)v$. Recall that, the interpolation functions of u and $u_{\mathcal{T}}$ are given by

$$Iu(v) = \sum_{i=1}^{2n} u(v_i) \psi_i(v) \quad \text{and} \quad Iu_{\mathcal{T}}(\mathcal{T}v) = \sum_{i=1}^{2n} u_{\mathcal{T}}(\mathcal{T}v_i) \psi_{i,\mathcal{T}}(\mathcal{T}v), \quad \forall v \in P, \quad (\text{C.3})$$

where $\{\psi_i\}_{i=1}^{2n}$ and $\{\psi_{i,\mathcal{T}}\}_{i=1}^{2n}$ are a set of QSE shape functions defined on P and $\mathcal{T}P$, respectively. Our QSE shape functions are linear combinations of the pair-wise products of MVCs with coefficients the ratios of oriented areas. Besides, MVCs are invariant with respect to P . Therefore, ψ_i and $\psi_{i,\mathcal{T}}$ are invariant with respect to domain P for $i \in \{1, 2, \dots, 2n\}$. By following Eq. (C.3), we have $Iu_{\mathcal{T}}(\mathcal{T}v) = Iu(v)$ for $\forall v \in P$. Thus, functions $u - Iu$ and $u_{\mathcal{T}} - Iu_{\mathcal{T}}$ are invariant with respect to P . By Theorem C.1 and Eq. (C.2), we have

$$\|u - Iu\|_{H^1(P)} = \|u_{\mathcal{T}} - Iu_{\mathcal{T}}\|_{H^1(\mathcal{T}P)} \leq C_e |u_{\mathcal{T}}|_{H^3(\mathcal{T}P)} = C_e \text{diam}(P)^2 |u|_{H^3(P)}. \quad \square$$

References

- [1] Y.J. Zhang, Geometric Modeling and Mesh Generation from Scanned Images, CRC Press, Taylor & Francis Group, 2016.
- [2] N. Sukumar, A. Tabarraei, Conforming polygonal finite elements, Int. J. Numer. Methods Eng. 61 (12) (2004) 2045–2066.
- [3] S.E. Leon, D.W. Spring, G.H. Paulino, Reduction in mesh bias for dynamic fracture using adaptive splitting of polygonal finite elements, Int. J. Numer. Methods Eng. 100 (8) (2014) 555–576.
- [4] D.W. Spring, S.E. Leon, G.H. Paulino, Unstructured polygonal meshes with adaptive refinement for the numerical simulation of dynamic cohesive fracture, Int. J. Fract. 189 (2014) 33–57.
- [5] I. Chiong, E.T. Ooi, C. Song, F. Tin-Loi, Scaled boundary polygons with application to fracture analysis of functionally graded materials, Int. J. Numer. Methods Eng. 98 (8) (2014) 562–589.
- [6] H. Chi, C. Talischi, O. Lopez-Pamies, G. H. Paulino, Polygonal finite elements for finite elasticity, Int. J. Numer. Methods Eng. 101 (4) (2015) 305–328.
- [7] E. Filipov, J. Chun, G. Paulino, J. Song, Polygonal multiresolution topology optimization (PolyMTOP) for structural dynamics, Struct. Multidiscip. Optim. 53 (2015).
- [8] M.S. Floater, Mean value coordinates, Comput. Aided Geom. Design 20 (1) (2003) 19–27.
- [9] A. Sinu, S. Natarajan, K. Shankar, Quadratic serendipity finite elements over convex polyhedra, Int. J. Numer. Methods Eng. 113 (1) (2018) 109–129.
- [10] I. Kovács, T. Várady, P-curves and surfaces: Parametric design with global fullness control, Comput. Aided Des. 90 (2017) 113–122, SI:SPM2017.
- [11] N. Sukumar, Quadratic maximum-entropy serendipity shape functions for arbitrary planar polygons, Comput. Methods Appl. Mech. Eng. 263 (2013) 27–41.
- [12] A. Rand, A. Gillette, C. Bajaj, Quadratic serendipity finite elements on polygons using generalized barycentric coordinates, Math. Comput. 83 (290) (2014) 2691–2716.
- [13] M.S. Floater, M.-J. Lai, Polygonal spline spaces and the numerical solution of the Poisson equation, SIAM J. Numer. Anal. 54 (2) (2016) 797–824.
- [14] H. Guo, E. Ooi, A. Saputra, Z. Yang, S. Natarajan, E. Ooi, C. Song, A quadtree-polygon-based scaled boundary finite element method for image-based mesoscale fracture modelling in concrete, Eng. Fract. Mech. 211 (2019) 420–441.
- [15] C. Talischi, G.H. Paulino, A. Pereira, I.F. Menezes, Polygonal finite elements for topology optimization: A unifying paradigm, Int. J. Numer. Methods Eng. 82 (6) (2010) 671–698.
- [16] J. Cao, Y. Xiao, Z. Chen, W. Wang, C. Bajaj, Functional data approximation on bounded domains using polygonal finite elements, Comput. Aided Geom. Design 63 (2018) 149–163.
- [17] X.-Y. Li, T. Ju, S.-M. Hu, Cubic mean value coordinates, ACM Trans. Graph. 32 (4) (2013) 126:1–10.
- [18] H.S.M. Coxeter, Introduction to Geometry, New York, London, 1961.
- [19] O. Weber, R. Poranne, C. Gotsman, Biharmonic coordinates, in: Computer Graphics Forum, Vol. 31, Wiley Online Library, 2012, pp. 2409–2422.
- [20] K. Hormann, N. Sukumar, Maximum entropy coordinates for arbitrary polytopes, in: Computer Graphics Forum, Vol. 27, Wiley Online Library, 2008, pp. 1513–1520.

- [21] X.-Y. Li, S.-M. Hu, Poisson coordinates, *IEEE Trans. Visual. Comput. Graph.* 19 (2) (2013) 344–352.
- [22] J. Zhang, B. Deng, Z. Liu, G. Patanè, S. Bouaziz, K. Hormann, L. Liu, Local barycentric coordinates, *ACM Trans. Graph.* 33 (6) (2014) 188.
- [23] M.S. Floater, Generalized barycentric coordinates and applications, *Acta Numer.* 24 (2015) 161–214.
- [24] Y. Lipman, D. Levin, D. Cohen-Or, Green coordinates, *ACM Trans. Graph.* 27 (3) (2008) 1–10.
- [25] P. Joshi, M. Meyer, T. DeRose, B. Green, T. Sanocki, Harmonic coordinates for character articulation, in: *ACM SIGGRAPH 2007 Papers*, in: *SIGGRAPH '07, Association for Computing Machinery*, New York, NY, USA, 2007, pp. 71–es.
- [26] M. Budninskiy, B. Liu, Y. Tong, M. Desbrun, Power coordinates: A geometric construction of barycentric coordinates on convex polytopes, *ACM Trans. Graph.* 35 (6) (2016) 241:1–11.
- [27] D. Anisimov, D. Panozzo, H. Kai, Blended barycentric coordinates, *Comput. Aided Geom. Design* 52–53 (MAR.–APR.) (2017) 205–216.
- [28] J. Tao, B. Deng, J. Zhang, A fast numerical solver for local barycentric coordinates, *Comput. Aided Geom. Design* 70 (MAR.) (2019) 46–58.
- [29] C. Deng, Q. Chang, K. Hormann, Iterative coordinates, *Comput. Aided Geom. Design* 79 (2020) 101861.
- [30] A. Quarteroni, A. Valli, *Numerical Approximation Of Partial Differential Equations*, Vol. 23, Springer Science & Business Media, 2008.
- [31] A. Rand, A. Gillette, C. Bajaj, Interpolation error estimates for mean value coordinates over convex polygons, *Adv. Comput. Math.* 39 (2) (2013) 327–347.
- [32] S. Dekel, D. Leviatan, The bramble–Hilbert lemma for convex domains, *SIAM J. Math. Anal.* 35 (5) (2003) 1203–1212.
- [33] G. Leoni, *A First Course in Sobolev Spaces*, American Mathematical Soc., 2017.
- [34] R.A. Adams, J.J. Fournier, *Sobolev Spaces*, Elsevier, 2003.
- [35] A. Gillette, A. Rand, C. Bajaj, Error estimates for generalized barycentric interpolation, *Adv. Comput. Math.* 37 (3) (2012) 417–439.
- [36] Y. Liu, W. Wang, B. Lévy, F. Sun, D.-M. Yan, L. Lu, C. Yang, On centroidal Voronoi tessellation-energy smoothness and fast computation, *ACM Trans. Graph.* 28 (4) (2009) 101:1–17.
- [37] D. Qiang, F. Vance, G. Max, Centroidal Voronoi tessellations: Applications and algorithms, *SIAM Rev.* 41 (4) (1999) 637–676.
- [38] Y. Xiao, Z. Chen, Z. Lin, J. Cao, Y.J. Zhang, Y. Lin, C. Wang, Merge-swap optimization framework for supervoxel generation from three-dimensional point clouds, *Remote Sens.* 12 (3) (2020) 473.
- [39] M.S. Ebeida, S.A. Mitchell, Uniform random voronoi meshes, in: W.R. Quadros (Ed.), *Proceedings of the 20th International Meshing Roundtable*, Springer Berlin Heidelberg, Berlin, Heidelberg, 2012, pp. 273–290.
- [40] G. Balafas, *Polyhedral mesh generation for cfd-analysis of complex structures*, Technical University Munich, 2014.
- [41] D. Sieger, P. Alliez, M. Botsch, Optimizing Voronoi diagrams for polygonal finite element computations, in: S. Shontz (Ed.), *Proceedings of the 19th International Meshing Roundtable*, Springer Berlin Heidelberg, Berlin, Heidelberg, 2010, pp. 335–350.
- [42] S. Lloyd, Least squares quantization in PCM, *IEEE Trans. Inf. Theory* 28 (2) (1982) 129–137.
- [43] J. Nocedal, Updating quasi-Newton matrices with limited storage, *Math. Comput.* 35 (151) (1980) 773–782.
- [44] J.-S. Chen, C.-T. Wu, S. Yoon, Y. You, A stabilized conforming nodal integration for Galerkin mesh-free methods, *Int. J. Numer. Methods Eng.* 50 (2) (2001).
- [45] S. Wandzurat, H. Xiao, Symmetric quadrature rules on a triangle, *Comput. Math. Appl.* 45 (12) (2003) 1829–1840.
- [46] D. Eberly, *Triangulation by ear clipping*, *Geom. Tools* (2008) 2002–2005.
- [47] Y. Krongauz, T. Belytschko, Consistent pseudo-derivatives in meshless methods, *Comput. Methods Appl. Mech. Eng.* 146 (3) (1997) 371–386.
- [48] K. Hormann, M.S. Floater, Mean value coordinates for arbitrary planar polygons, *ACM Trans. Graph.* 25 (4) (2006) 1424–1441.